IMAGE FORMATION IN A γ-RAY COMPTON BACKSCATTERING DEVICE

Luisa Natalia González Gómez

Universidad Nacional de Colombia
Facultad de Ciencias
Departamento de Física
Bogotá, D.C.
2013

IMAGE FORMATION IN A γ-RAY COMPTON BACKSCATTERING DEVICE

Luisa Natalia González Gómez

Thesis submitted for the degree of
Maestría en Ciencias-Física

Advisor
Fernando Cristancho Mejía

Research group
Grupo de Física Nuclear

Universidad Nacional de Colombia
Facultad de Ciencias
Departamento de Física
Bogotá, D.C.
2013

Title in English

Image formation in a γ-ray Compton backscattering device

Título en español

Formación de imágenes en un dispositivo de retrodispersión Compton de rayos γ

Abstract: The Compton Camera is a backscattering device that allows us to obtain images of hidden objects. The device includes a ^{22}Na source placed in a conical lead shielding and two geometrically opposing CsI detectors, one position sensitive detector in charge of building the image and a backscattering detector in charge of triggering the recollection of data. In order to study the image formation in the device we developed a theoretical approximation to evaluate the backscattered intensity as a function of depth. We have performed backscattering experiments to analyze the number of single and multiple backscattered photons as a function of thickness and to compare the experimental results with the theoretical model. The results of this comparison show that Multiple Compton events have a detrimental effect on the quality of the image and the Single Compton events build the image. We have evaluated the differences in backscattered intensity between two different materials to study the contrast in the image obtained.

Resumen: La cámara Compton es un dispositivo que nos permite obtener imágenes de objetos enterrados. El dispositivo está compuesto de una fuente de ^{22}Na puesta en un blindaje cónico de plomo y dos detectores de CsI, uno de ellos es un detector sensible a posición encargado de construir la imagen, el otro es el detector de retrodispersión encargado de obtener la señal de energía. Para estudiar la formación de la imagen en el dispositivo se desarrolló una aproximación teórica para evaluar la intensidad retrodispersada como función de la profundidad. Se desarrollaron experimentos de retrodispersión para analizar el número de fotones retrodispersados como función de la profundidad y comparar con el modelo teórico. Los resultados de está comparación muestran que los fotones que realizan dispersiones múltiples tienen un efecto negativo en la calidad de la imagen y los fotones que realizan una sola dispersión Compton contruyen la imagen. Se han evaluado las diferencias en la intensidad retrodispersada entre dos materiales para estudiar el contraste en la imagen obtenida.

Keywords: Compton Camera, γ-ray, Backscattering, Imaging formation

Palabras clave: Cámara Compton, Rayos γ, Retrodispersión, Formación de imágenes

Contents

List of Tables

List of Figures

Introduction

Using the transmission of X and γ-rays it has been possible to obtain images of objects like human bodies and casting objects, since already a long time (Figure 1 a)). The next technical challenge is to use the same radiation and obtain images in a backscattering set-up (Figure 1 b)) when is impossible to put the sample between source and detector for example in biomedical science [1], applications in the food processing industry, with the aim of detecting contaminants in foodstuffs [2] and detection of explosives in airport baggage [3]. This technique, known as Gamma-ray Compton Backscattering (GBT) is able to produce images of objects buried to a depth around 7 cm by sending a beam of gamma-rays towards the sample of soil under inspection and obtaining an image of the sample with the backscattered radiation [4]. The Grupo de Física Nuclear de la Universidad Nacional de Colombia (gfnun) has already made progress towards the mastering of the technique including basic research on the interaction γ-soil and the operation of an imaging prototype device called "Compton Camera" which has proved effective in laboratory tests since images of objects buried in soil have already been obtained.

We follow up in the present work the research reported in Reference [5] where it was shown that such an imaging device has photographic characteristics since an image is obtained directly from the readout of a CsI detector with a position-sensitive photomultiplier, and very importantly, without any additional image processing. A simplified schema of "Compton Camera" working principle is in Figure 2. It uses a ^{22}Na γ-source placed within a conical lead shielding. In the top of the shielding is placed a position-sensitive detector. A ring-shaped detector is enclosing the source and is used as a backscattering detector. ^{22}Na emits positrons which rapidly annihilate with electrons. The annihilation of each electron-positron pair produces two γ-rays of 511 keV traveling in opposite directions. One of these photons can be detected in the position detector, a CsI crystal coupled to a position-sensitive photomultiplier. The other γ-ray goes into the soil where it can be absorbed or backscattered. If the photon is backscattered it can be detected in the backscattering detector. The device produces an image with the backscattered γ-rays counted in the position detector in coincidence with the other detector. The image is built because both Compton backscattering probability and photoelectric absorption depend on the electron density of the matter in front of the device. The

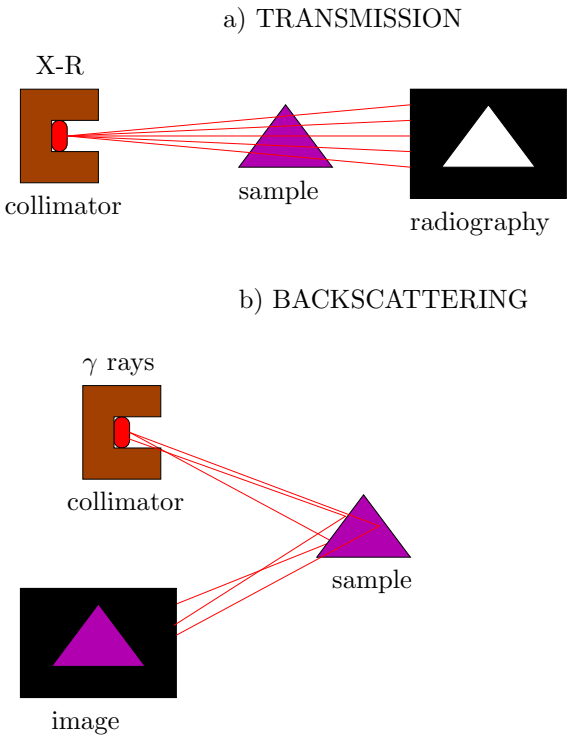

FIGURE 1. Difference between images obtained by backscattering and transmission

result of a measurement is a bidimensional matrix in which the values in each point is the number of collected photons in the corresponding pixel, $f(x, y)$.

To obtain first images with the "Compton Camera" the adjustable electronic settings of the photomultipliers attached to backscattering detector were investigated [6]. The device's characterization was performed in order to evaluate the quality of the images obtained when varying geometric parameters such as stand off distances and electronic parameters like the threshold voltages of the two detectors (backscattering and position) [7]. Experiments were carried out to determine the response of the Compton Camera to materials like water, sand, paraffin, paper, lead, polystyrene and air. Mathematical methods that strive to give a numerical value to the image quality and to the device's capability of distinguishing different materials were developed [8]. Theoretical and experimental work has investigated whether different types of soil (sand and farming soil) produce different spectroscopic distributions of the backscattered radiation as a function of the thickness and water content of the sample [9, 10, 11, 12]. It is clear that the processes generating the spectroscopic characteristics of the backscattered radiation need to be investigated along with the processes that take place once this radiation interacts with the "Compton Camera".

In order to understand the formation of the image in the Compton Camera we have performed independent experiments specifically planned to quantify the backscattering capabilities of different materials. The present work presents the

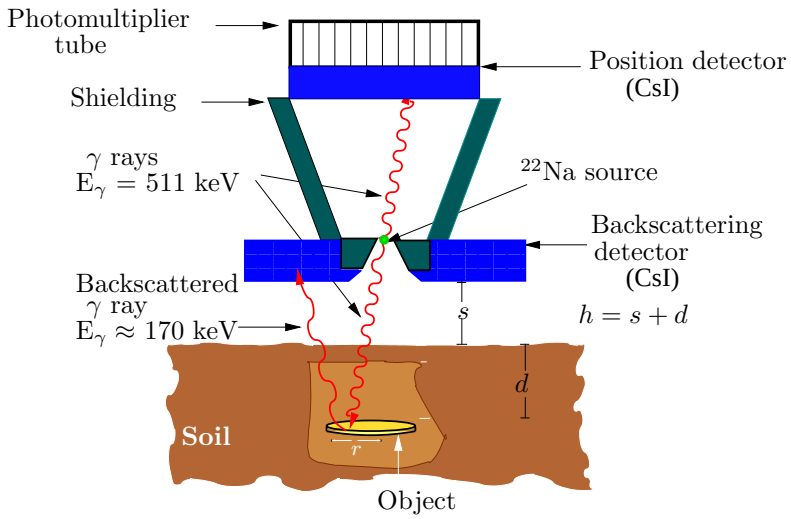

FIGURE 2. Working principle of the Compton Camera.

study of the interaction of γ-rays with sheets of aluminum and iron. The experimental setup to make spectroscopy on the backscattered γ-rays from a monoelemental material mimics the geometry and electronics of the "Compton Camera". The two γ-rays are provided also here by a ^{22}Na source; a Ge plays the role of Backscattering Detector and the plastic one acts as Position Detector. Backscattered spectra are analyzed in order to obtain information about the interaction processes and to study the conditions under which materials of different composition can be distinguished by the camera and the contrast concept in the image. Using the same experimental set-up we can study the backscattering of γ rays from the surface of a material, it allows us to study degradation processes such as wear and corrosion in industries machines, pipes and other materials [13] and to test steel quality in the manufacture of cars and to obtain the proper thickness of tin and aluminum [14].

In Chapter 1 a review of models on the interaction of radiation with matter and general properties of detection system will be made. In Chapter 2 the theoretical model to study the backscattered intensity as a function of thickness is explained. In Chapter 3 the experimental setup, regarding geometry and electronics will be described. In Chapter 4 is shown the results obtained, the analysis performed on the backscattering spectra and the comparison between the experimental results with the theoretical.

CHAPTER 1

Theoretical Background

1.1 Interaction of radiation with matter

The photon interaction on atoms or on atomic electrons results in a change of the incoming photon energy and the direction of the scattered photons. Atomic electrons can be extracted after the full or the partial absorption of the primary photon. The main competing and energy dependent processes contributing to the total cross section are:

- The photoelectric effect in which the interaction takes place with the entire atomic electron cloud and results in the complete absorption of the primary photon energy.
- Compton scattering on atomic electrons at photon energies so that the electron binding energies can be neglected and electrons can be treated as quasi-free.
- Pair production in which the photon incoming energy is high enough to allow the creation of an electron-positron pair in the Coulomb field of a nucleus.

The photoelectric process dominates at low energies, below 50 keV for aluminum and 500 keV for lead. As the energy increases, between 0.05 and 15 MeV for aluminum and between 0.5 and 5 MeV for lead, the main contribution to the attenuation coefficient comes from Compton scattering. At larger energies, pair production becomes the dominant mechanism of photon interaction with matter.

In the **photoelectric effect** the photons whose energy E_γ is larger than the binding energies (B_e) of atomic electrons, can be completely absorbed in the interaction with an atom, which in turn emits an electron raised into a state of the continuous spectrum. In the interaction, the entire cloud, rather than the individual electron, is involved, while the atom, as a whole, takes up the quite small recoil energy to

preserve momentum and energy. Thus, the kinetic energy E_k of the electron after leaving the atom is determined by

$$E_k = E_\gamma - B_e \tag{1.1}$$

Since a free electron cannot absorb a photon, we should expect that the photoelectric absorption probability is larger for more tightly bound electrons, for K-shell electrons. In fact, for incoming photon energies larger than K-shell energies, more than about 80% of the photoelectric absorption occurs involving the emission of K-shell electrons. If the photon energy is lower than the binding energy of a shell, an electron from that shell cannot be emitted. Therefore, the absorption curve (Figure 1.1) shows the characteristic absorption edges, whenever the incoming photon energy coincides with the ionization energy of electrons of K, L, M, ... shells.

The exact theoretical calculations of the photoelectric effect present difficulties and

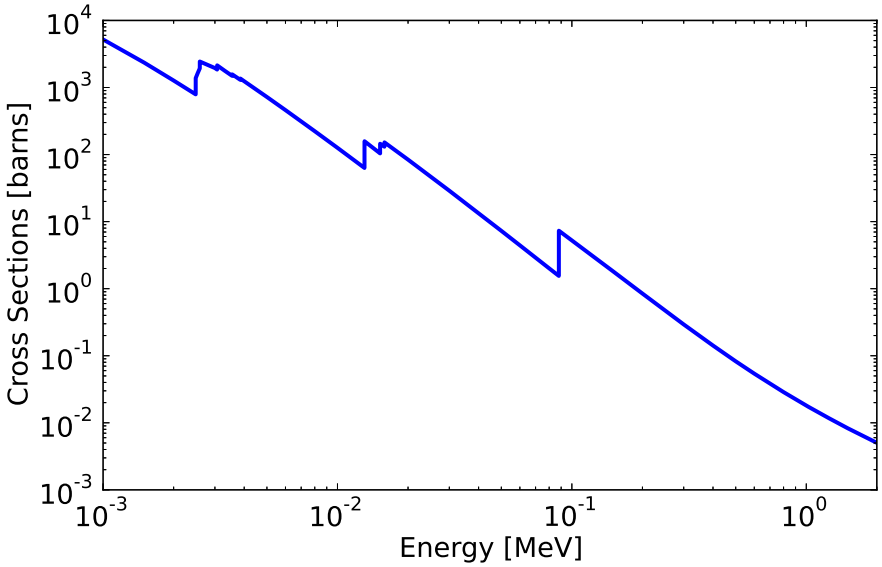

FIGURE 1.1. Photoelectric cross sections for lead as a function of incident photon energy [15]

usually empirical expressions are used for computing the total (σ) and K-shell cross sections per atom. In the non-relativistic region for $E_\gamma \ll mc^2$ where m is the rest mass of the electron and when the incoming photon energies are large compared with the ionization energy of the K-shell electrons, the *Born's approximation* can be used. The angular distribution of the emitted electrons is expressed by the K-shell differential cross section per atom

$$\sigma_{ph} = 4\sigma_0\alpha^4\sqrt{2}Z^5\left(\frac{mc^2}{E_\gamma}\right)^{7/2}, \tag{1.2}$$

where Z is the atomic number of the material, $\sigma_0 = \frac{8}{3}\pi r_e^2$. It is important to note that the total photoelectric cross section depends on the atomic number Z to a

power close to 5, then, the higher Z materials are the most favored for photoelectric absorption.

The **Compton effect** is an incoherent scattering process on individual atomic electrons. These electrons can be described as quasi-free, i.e., in first approximation their binding energies do not affect the interaction. Furthermore, it is considered as an inelastic process, although the kinematics description of the reaction can be treated like an elastic collision. The scattered photon energy depends on the photon scattering angle θ as we can see in Figure 1.2 and is related to the incoming photon energy.

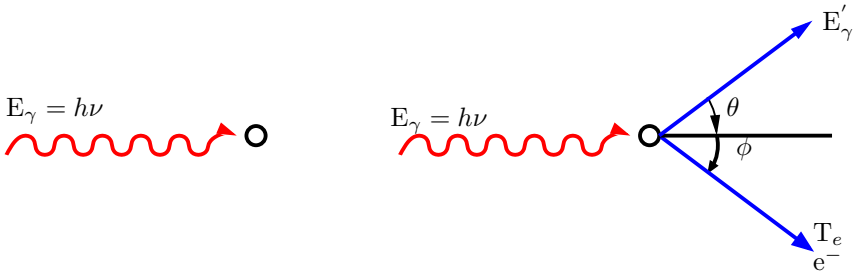

FIGURE 1.2. Compton scattering of an incident photon with incoming energy E_γ onto a quasi-free electron which emerges at an angle ϕ. θ is the angle between the direction of the incident photon and the photon scattering direction.

The relation between the energy of the scattered photon E'_γ and the scattering angle is

$$E'_\gamma = \frac{E_\gamma}{1 + \epsilon(1 - \cos\theta)}, \tag{1.3}$$

where $\epsilon = E_\gamma/(mc^2)$ is the reduced energy of the incoming photon. The differential cross section for Compton scattering of a photon interacting on a quasi-free electron is given by the called Klein Nishina equation [16]:

$$\frac{d\sigma_C}{d\Omega} = \frac{r_e^2}{2}\frac{1}{[1 + \epsilon(1 - \cos\theta)]^2}\left(1 + \cos^2\theta + \frac{\epsilon^2(1 - \cos\theta)^2}{1 + \epsilon(1 - \cos\theta)}\right) \tag{1.4}$$

where r_e is the electron classical radius.

When the incoming photon energy exceeds twice the energy corresponding to the electron rest mass $2mc^2 \approx 1.02$ MeV, the production of an electron and positron pair becomes possible (Figure 1.3). The process of the **pair production** can only occur close to a charged massive object (for instance a nucleus) which takes away the amount of momentum needed to preserve momentum conservation, during the interaction with the Coulomb field of the massive object itself. The pair production process becomes the dominant mechanism for photon interaction in matter above 2

MeV and accounts for almost the whole γ-ray absorption in this energy range [12].

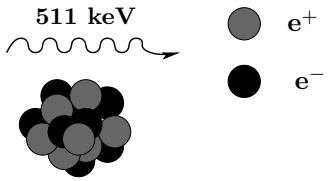

FIGURE 1.3. An incoming photon interacts with the Coulomb field of a massive nucleus.

1.2 Total attenuation coefficient

The total number of backscattered photons is mainly the combination of two effects: the γ-ray beam attenuation ($\mu = \mu_C + \mu_{ph}$) and the scattering probability (μ_C). The total interaction cross section for the photon is the sum of individual cross sections for each of the effects described previously. The total cross section by atom will be:

$$\sigma_T = \sigma_{ph} + Z\sigma_C + \sigma_{pp} \tag{1.5}$$

where σ_{ph} is photoelectric effect cross section, σ_C the Compton effect cross section and σ_{pp} the pair production effect cross section.

The linear attenuation coefficient is obtained if we multiply the electronic density $n = N_A\rho/w$ by Equation (1.5). This coefficient gives us the probability for γ-rays to interact with any material as a function of energy,

$$\mu = \frac{N_A\rho}{w}\sigma \tag{1.6}$$

where N_A is the Avogadro's number, ρ is the density of the sample and w is its molecular weight. Then Equation (1.6) is the relation between the density of the sample with the linear attenuation coefficient. However, two samples that have the same composition but they are in different physical state (gas, liquid and gaseous) have different value of μ, so the mass attenuation coefficient μ/ρ is the quantity most useful in graphs representations because this is independent of the physical state of the sample.

Figure 1.4 shows the mass attenuation coefficient for the interaction γ-aluminum for each of the possible processes. For energies less than 0.511 MeV the highest interaction probability is photoelectric effect, in the region marked by the dotted lines the most probable interaction is the one corresponding to Compton effect. For energies bigger than 1.274 MeV the pair production dominates the interaction.

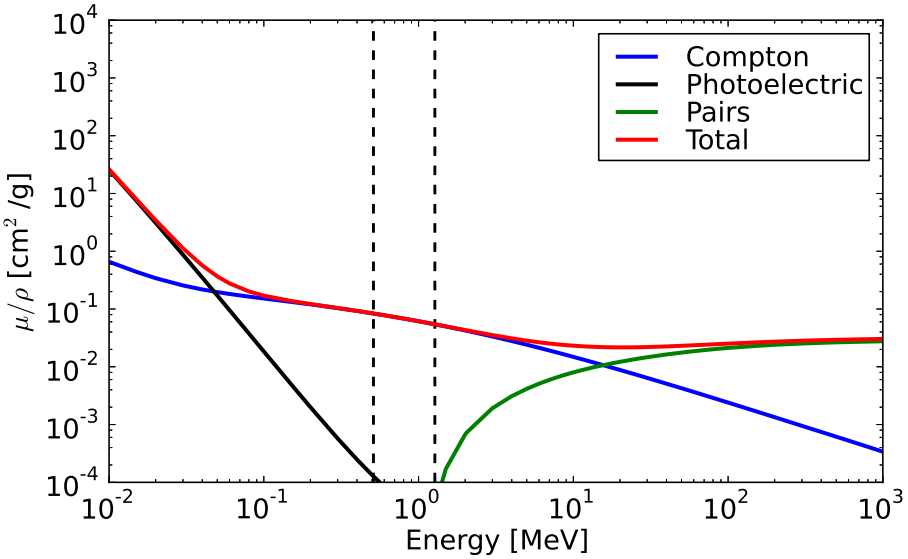

FIGURE 1.4. Total mass attenuation coefficient for the interaction of γ-rays with aluminum (red line). The blue line corresponds to the Compton effect cross section, the black line represents the photoelectric effect cross section and the green line corresponds to the pair production cross sections [15].

The intensity of the transmitted radiation trough a sample decreases exponentially with the sample's thickness, x,

$$I = I_0 \exp(-\mu x) \tag{1.7}$$

where I_0 is the initial intensity. However, there are an increase in the intensity of the transmitted radiation due to the photons that perform multiple dispersions known as buildup factor $B(x)$,

$$I = I_0 B(x) \exp(-\mu x) \tag{1.8}$$

$B(x)$ factor depends on the geometry of the experimental arrangement and the sample's properties.

1.3 The scattering probability

The scattering probability of a photon of incident energy E_γ in a solid angle $d\Omega$ around an angle θ as a function of the scattering angle is given by the Klein-Nishina formula, Equation (1.4). Figure 1.5 shows a polar plot of the Klein-Nishina formula for different incident energies, where p_γ represents the momentum of the γ-ray, the arrow indicates the photon incidence direction and the center is the point of collision between photon and electron. We can see from the Figure that there is a strong

tendency to forward scattering for all energies. In fact, as energy increases the backscattering probability decreases rapidly.

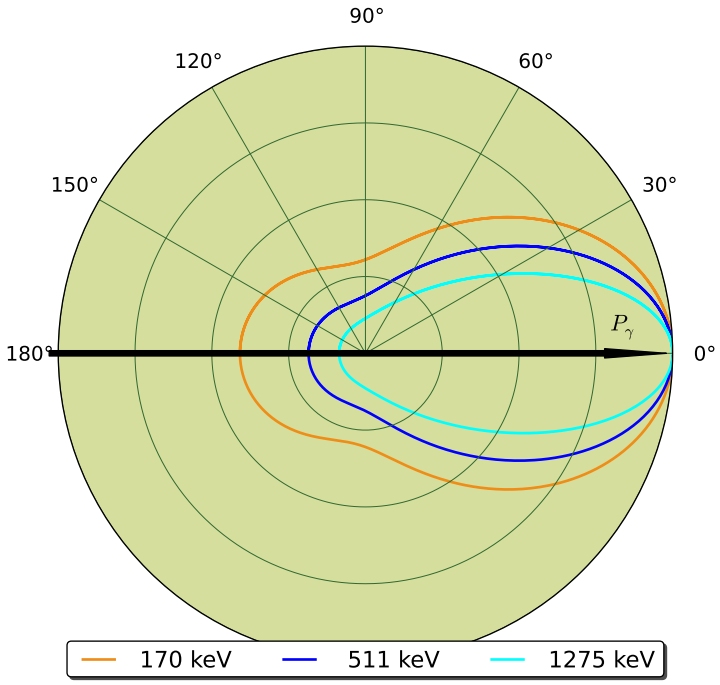

FIGURE 1.5. Polar plot of the Klein-Nishina formula for different incident energies. The radius of the plot represents the probability for the photon to be scattered in each angle.

1.4 Detectors

All radiation detectors are based on the same fundamental principle: the transfer of part or all of the radiation energy to the detector mass where it is converted into some other form more accessible to human perception. The form in which the converted energy appears depends on the detector and its design. The gaseous detectors are designed to directly collect the ionization electrons to form an electrical current signal, while in scintillators both the excitation and ionization contribute to inducing molecular transitions which result in the emission of light.

1.4.1 Scintillation detectors

A scintillation detector consists of a scintillating material in which large fractions of incident energy carried by striking particles or radiation are absorbed and transformed into detectable photons visible or near visible light. The photons emitted in such detectors must be transported, by light guides, to photo-sensitive

devices, like photomultipliers, to be collected. As radiation passes through the scintillator, it excites the atoms and molecules causing the light is emitted. This light is transmitted to the photomultiplier where it is converted into a weak current of photoelectrons which is then further amplified by an electron multiplier system. The resulting current signal is the analyzed by an electronics system.

- **Plastic scintillators**

  Plastic scintillators are typically a scintillating material in which the primary fluorescent emitter, called a fluor, is suspended in the base, a solid polymer matrix. While this combination is typically accomplished through the dissolution of the fluor prior to bulk polymerization, the fluor is sometimes associated with the polymer directly, either covalently or through coordination, as is the case with many ^{6}Li plastic scintillators. Polyethylene naphthalate has been found to exhibit scintillation by itself without any additives and is expected to replace existing plastic scintillators due to higher performance and lower price [17]. The advantages of plastic scintillators include fairly high light output and a relatively quick signal, with a decay time of 2-4 nanoseconds, but perhaps the biggest advantage of plastic scintillators is their ability to be shaped, through the use of molds or other means, into almost any desired form with what is often a high degree of durability [18].

- **Organic scintillators:** Organic scintillators are aromatic hydrocarbon compounds containing a benzenic cycle. In organic scintillators, the mechanism of light emission is a molecular effect. It proceeds through excitation of molecular levels in a primary fluorescent material which emits bands of ultraviolet (UV) light during de-excitation. This UV light is absorbed in most organic materials with an absorption length of a few mm.

- **Inorganic scintillators:**

  Inorganic scintillators are ionic crystals doped or not with activators. Production of luminescence in organic scintillator such as NaI(Tl) or CsI(Tl) requires the presence of an activator like Thalium. Inorganic scintillators have high density and high atomic number compared to organic scintillators. From these properties, one can immediately expect the inorganic scintillators to have high absorption for γ and X-rays. They also have high absorption for electrons, alpha, protons and charged heavy particles, in general.

1.4.2 Semiconductor detectors

Solid state detectors are made from semiconductor materials. These are characterized by a small gap between the electronic conduction band and the valence band. In the case of silicon, an energy $E_g = 1.12$ eV is needed to excite an electron from the valence band into the conduction band. For

comparison, $E_g > 5$ eV for insulators and conductors have their valence and conduction bands in contact.

In these detectors, radiation is measured by means of the number of charge carriers set free in the detector, which is arranged between two electrodes. Ionizing radiation produces free electrons and holes. The number of electron-hole pairs is proportional to the intensity of the radiation to the semiconductor. As a result, a number of electrons are transferred from the valence band to the conduction band, and an equal number of holes are created in the valence band. Under the influence of an electric field, electrons and holes travel to the electrodes, where they result is a pulse that can be measured in an outer circuit. The holes travel in the opposite direction and can also be measured. As the amount of energy required to create an electron-hole pair is known, and is independent of the energy of the incident radiation, measuring the number of electron-hole pairs allows the intensity of the incident radiation to be found.

The advantage of semiconductor detectors is their good energy resolution. For a Ge detector, the FWHM at 1000 keV is around 2 keV, thus having a resolution of 0.2%. On the other hand, its efficiency is not so high as the efficiency of some scintillators. The relative efficiency of a germanium detector, defined as the ratio between the number of counts recorded when placing a ^{60}Co source 25 cm away from the detector and the counts recorded by a Na(Tl) under the same conditions, is about 40%. The timing characteristics of semiconductors are determined by the charge collection mechanism. As charge carriers must travel to the corresponding electrode, the time needed to completely collect the charge produced by a γ-ray depends on the position in the crystal where the photon interacted, thus, each output pulse has a different form. A typical time for signals in a Ge detector to be collected is about 120 ns, making this detector a very slow one [19].

1.5 General Characteristics of detectors

1. **Energy Resolution:** Is the capability to distinguishing two energies lying close to each other. The resolution can be measured by sending a monoenergetic beam of radiation into the detector and observing the resulting spectrum. In the ideal case one would like to see a sharp delta-function peak, but real detectors produces a peak structure with a finite width, usually Gaussian in shape characterized by the Full Width at Half Maximum (FWHM). The resolution of a detector at the energy Eγ is defined as:

$$\text{Resolution} = \frac{\text{FWHM}}{E_\gamma} \tag{1.9}$$

For γ-rays about 1 MeV, a NaI detector has about a 8% or 9% resolution while germanium detectors have resolutions on the order of 0.1%. In Figure 1.6 is shown a comparison between the experimental spectra obtained with HPGe and NaI detectors when detecting an energy of 511 keV.

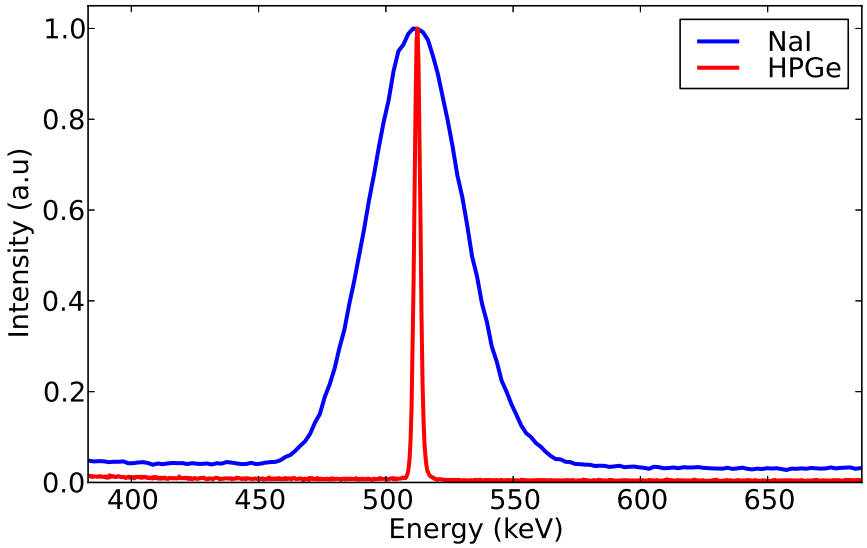

FIGURE 1.6. Comparison between the energy resolution of a NaI (green line) and of a Germanium detector (red line) for an incident energy of 511 keV.

2. **Detector efficiency:** The total or absolut efficiency of a detector is defined as that fraction of events emitted by the source which is actually registered by the detector:

$$\epsilon_{\text{total}} = \frac{\text{events registered}}{\text{events emitted by the source}} \tag{1.10}$$

This is a function of the detector geometry and the probability of an interaction in the detector. The intrinsic efficiency is that fraction between the events registered by the detector and the fraction of photons emitted by the source that reach the volume of the detector as

$$\epsilon_{\text{intrinsic}} = \frac{\text{events registered}}{\text{events impinging on detector}} \tag{1.11}$$

This probability depends on the interaction cross sections of the incident radiation on the detector medium. The intrinsic efficiency is thus a function of the type of radiation, its energy and the detector material. The geometry efficiency is that fraction of the source radiation which is geometrically intercepted by the detector. Then this depends entirely on the geometrical configuration of the detector and source and the angular distribution of the incident radiation [20].

CHAPTER 2

Theoretical model

2.1 Backscattering intensity

In order to study the formation of the image in the Compton Camera and to understanding why is possible to obtain images using γ-rays we make use of a simple single backscattering model that helps us to estimate the intensity of the backscattered photons as a function of the material thickness and allows us to evaluate if it is possible to have contrast in images of two different material objects.

The number of backscattered photons depends on the Compton backscattering probability and photoelectric absorption probability. So as to compare two different materials and to estimate the number of backscattered photons, it is necessary to evaluate the two probabilities.

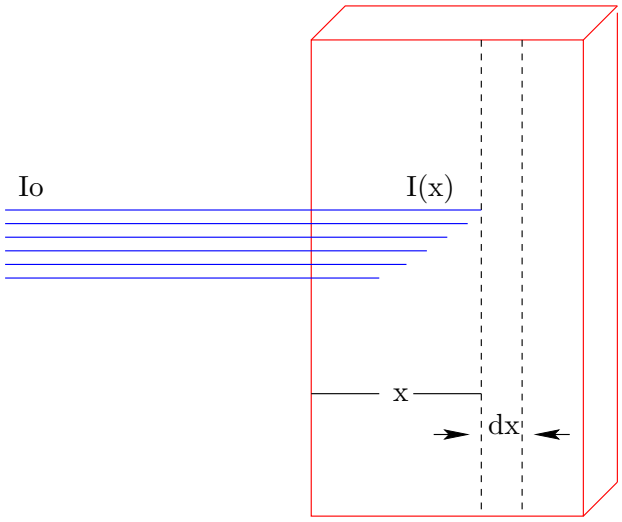

FIGURE 2.1. Without taking into account buildup, the intensity at x depends on the total absortion coefficient as $I(x) = I_0 e^{-\mu x}$.

The initial intensity is I_0; $I(x)$ is the number of photons after traveling x, and we want to know how many of these photons are backscattered in x as shown in Figure 2.1. The transmitted intensity taking into account the Compton scattering and photoelectric absorption is given by

$$I(x) = I_0 \exp(-\mu_1 x) \tag{2.1}$$

where $\mu_1 = \mu_{ph1} + \mu_{C1}$ for $\mathrm{E}_\gamma = 511$ keV.

From I_0 photons that begins the travel just $R(x)$ will arrive to the detector. The backscattering probability in dx is proportional to $\mu_{C1}dx$. This proportionality is just because $\mu_{C1}dx$ accounts for the photons scattered in all directions. Therefore, if the solid angle of the detector ($\Delta\Omega$), is not too large:

$$w = \mu_{C1}dx\frac{\Delta\Omega}{4\pi}. \tag{2.2}$$

Hence, the number of backscattered photons on x will be:

$$R(x) = \frac{\Delta\Omega}{4\pi}\mu_{C1}I_0 \exp(-\mu_1 x)dx \tag{2.3}$$

Let us suppose that all arrived photons on x are scattered in a 180 ° angle, then, it final energy, according to Equation 1.3 will be $E_\gamma = 170$ keV. Of the $R(x)$ photons that start the travel back at x, only a fraction $dI_B(x)$ reach the detector.

$$dI_B(x) = R(x) \exp(-\mu_2 x) \tag{2.4}$$

where $\mu_2 = \mu(E_\gamma = 170.3\,\mathrm{keV})$

Replacing Equation (2.3) in Equation (2.4) we have

$$dI_B(x) = \frac{\Delta\Omega}{4\pi}\mu_{C\,1}I_0 \exp[-(\mu_1 + \mu_2)x]dx. \tag{2.5}$$

Integrating over x we have a first approximation,

$$I_B(x)(x) = \frac{\Delta\Omega}{4\pi}I_0\mu_{C\,1}\int_{x'=0}^{x'=x} \exp[-(\mu_1 + \mu_2)x']dx' \tag{2.6}$$

$$= \frac{\Delta\Omega}{4\pi}.\frac{\mu_{C\,1}}{\mu_1 + \mu_2}\{1 - \exp[-(\mu_1 + \mu_2)x]\}. \tag{2.7}$$

As first approximation let us consider the quantity in the Equation (2.8). The $4\pi/\Delta\Omega$ term is related to detection system's geometrical properties, $\mu_{C\,1}/(\mu_1 + \mu_2)$ term is related to physical properties of material. Now, using values from know data-bases [15], we can see the behaviour of $I_B(x)$ for different materials.

$$\frac{4\pi}{\Delta\Omega}\frac{I_B(x)}{I_0} = i_B(x) = \frac{\mu_{C\,1}}{\mu_1+\mu_2}\{1-\exp[-(\mu_1+\mu_2)x]\} \tag{2.8}$$

2.2 Materials

We can divide the materials to be studied in three groups: the first are organics materials: materials that contain hydrogen, oxygen and carbon. The other group are monoelemental metals like copper, aluminum, lead and tungsten and the third group is composed by polyelemental materials like steel and concrete. We are focused in the study of steel and concrete because these gives us knowledge about civil engineering in facts like structural damage on concrete wall and to evaluate the backscattering capability from some elements.

We make a compilation in Table 2.1 of the physical quantities ρ (density), μ (linear attenuation coefficient), λ (mean free path), for the three principal groups of materials described above. $\langle Z\rangle$ [20] in Table 2.1 was calculated following:

$$\langle Z\rangle = \sum a_i Z_i \tag{2.9}$$

The mean free path (λ) is the average distance traveled by the photon before it interacts. Is given by the inverse of linear attenuation coefficient (Equation 1.6). The results in the last column of Table 2.1 suggest that in the case of very thick targets, water backscatters 8 times more than lead. Using the quantities calculated in the Table 2.1 we can define the Contrast like the difference in backscattered intensity i_B between two close-by surfaces. I.e, if we want to obtain images with Compton Camera, we have to check the backscattering capability belonging to each interest material. In the present work we used aluminum and iron to demonstrate experimentally Equation 2.8.

To have an idea about orders of magnitude let us consider the extreme situations of very thin and very thick target.

- Very thin target: For

$$\Delta x << \frac{1}{\mu_1+\mu_2} = \lambda_1+\lambda_2 \tag{2.10}$$

  According to Table 2.1 $\lambda_1 \approx \lambda_2 \approx 0.1$ cm - 1.0 cm for Si_2O and H_2O which implies that "thin target" means thickness in the tenths of mm for organic materials. Expanding in Taylor-series the Equation 2.8

$$i_B(x) = \mu_{C1}\Delta x \tag{2.11}$$

Materials	Stoichometry	$\langle Z \rangle$	ρ (g/cm^3)	λ (cm)	$\frac{\mu_{C1}}{\mu_1 + \mu_2}$
Sand	See Table A.1	15.0	1.58	7.74	0.39919
Water	H_2O	5.0	1.00	10.44	0.40153
Paper	$C_6H_{10}O_5$	25.5	1.15	9.50	0.40173
Paraffin	$C_{20}H_{42}$	81.0	0.95	10.64	0.40176
Soil	See Table A.2	14.6	1.50	9.81	0.39294
Copper	Cu	29.0	8.96	1.38	0.31128
Aluminum	Al	13.0	2.70	4.45	0.39714
Lead	Pb	82.0	11.35	0.60	0.04328
Tungsten	W	74.0	19.35	0.41	0.05606
Concrete	See Table A.3	120.1	2.30	5.05	0.38608
Steel	Fe_3C [15]	39.0	8.00	1.52	0.33994
Iron	Fe	26.0	7.87	1.55	0.33595

TABLE 2.1. Calculated physical values for differents materials.

- Very thick target: For

$$\Delta x >> \frac{1}{\mu_1 + \mu_2} = \lambda_1 + \lambda_2 \tag{2.12}$$

In Equation 2.8 the term $\exp(-[\mu_1 + \mu_2]) \to 0$ therefore:

$$i_B(\infty) = \frac{\mu_{C1}}{\mu_1 + \mu_2} \tag{2.13}$$

It is important to observe that $i_B(\infty)$ can be calculated either with the linear or the mass attenuation coefficients since the density dependence cancels out.

2.2.1 Attenuation coefficients

Figures 2.2, 2.3, 2.4 shows the mass attenuation coefficients as a function of energy for the three groups of materials and for each one of the processes of interaction. In Figures the red vertical lines mark E_γ=511 keV which is the energy of incident γ ray and E_γ=170 keV which is the energy of backscattered photon. The highest interaction probability for all materials is the one corresponding to Compton effect.

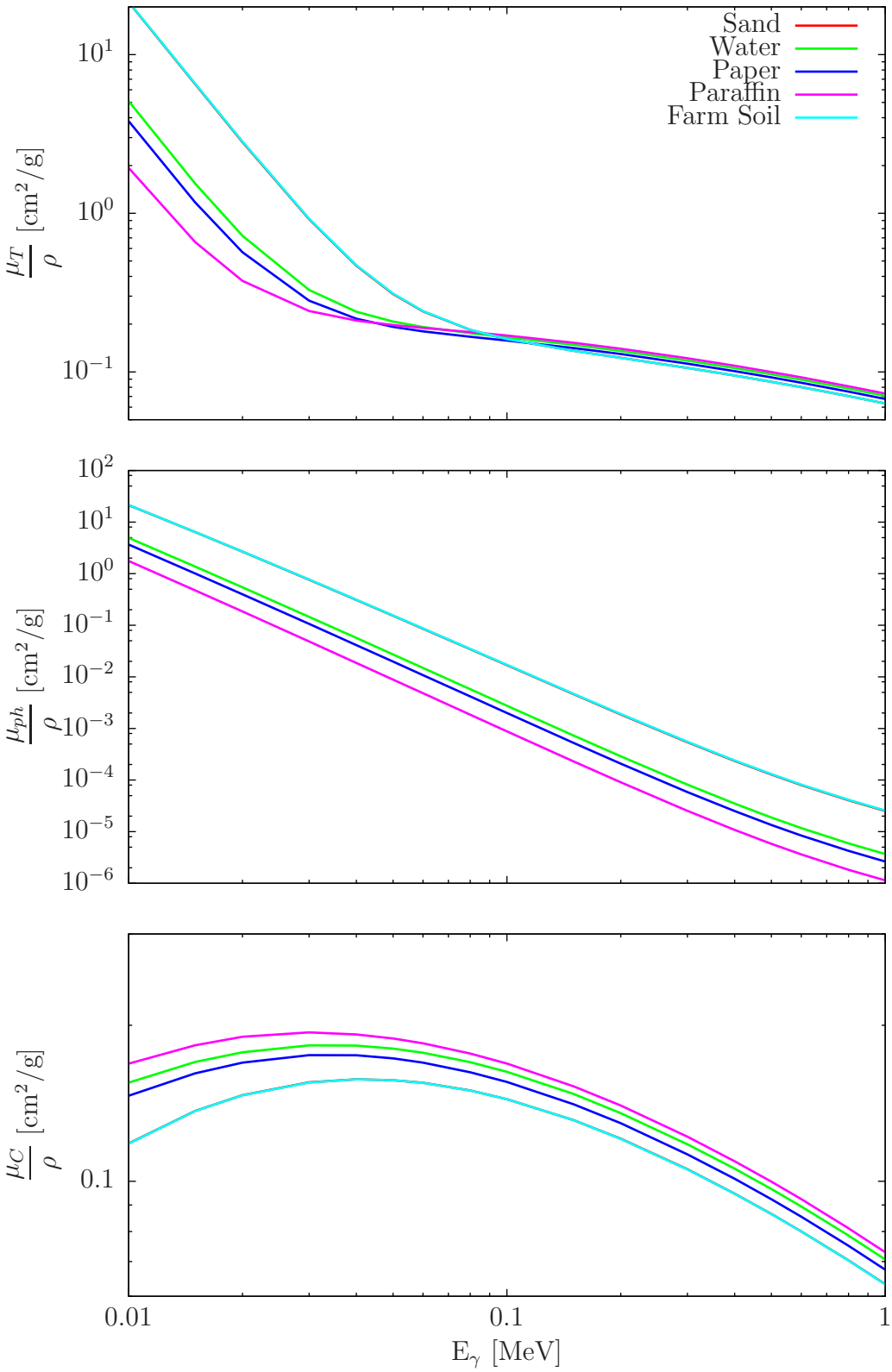

FIGURE 2.2. Mass attenuation coefficient for organic materials. Red vertical lines mark E_γ=170 keV (backscattering at $\theta = 180°$) and E_γ=511 keV [13].

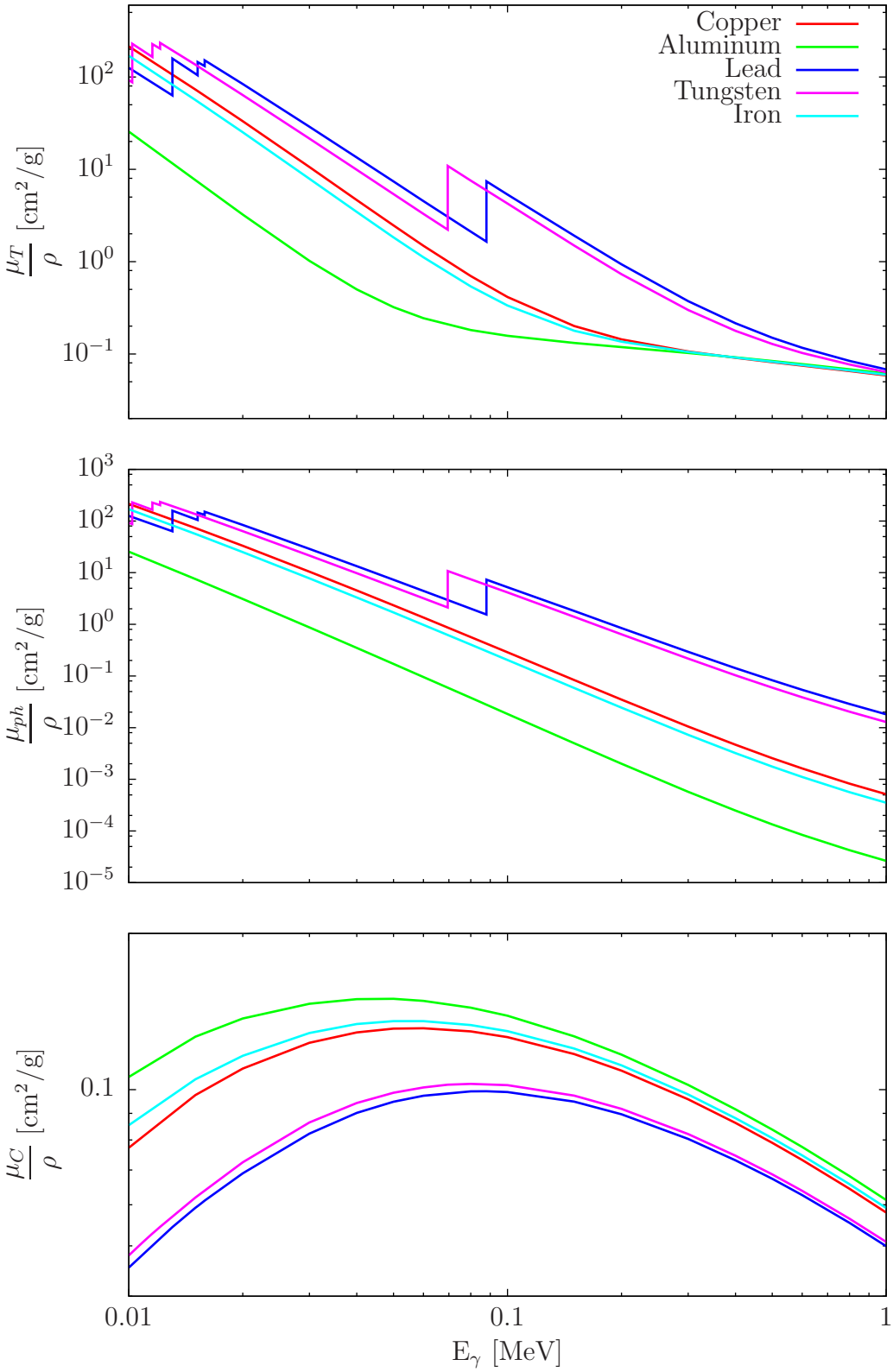

FIGURE 2.3. Mass attenuation coefficient for elements. Red vertical lines mark E_γ=170 keV (backscattering at $\theta = 180°$) and E_γ=511 keV [13].

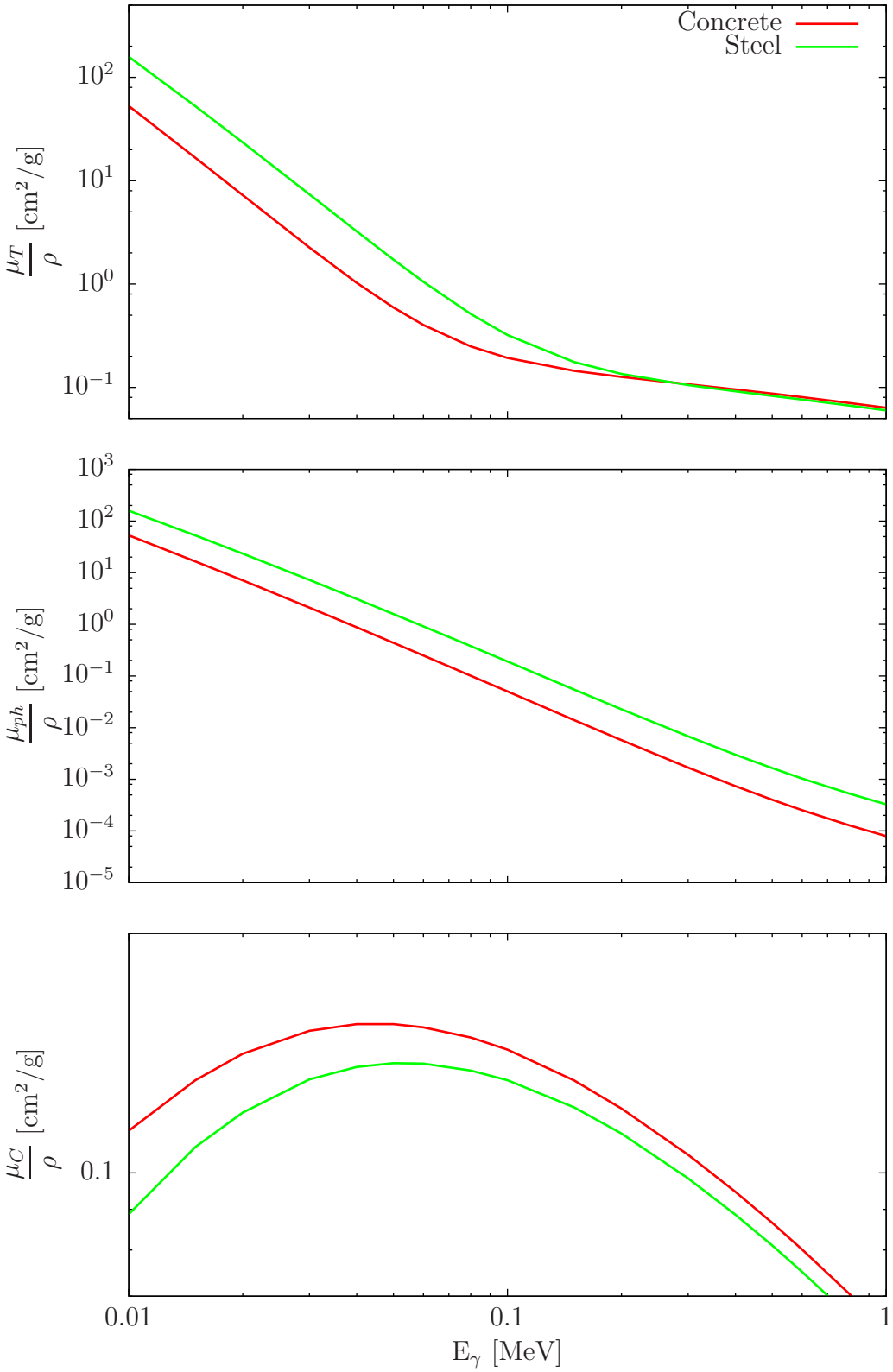

FIGURE 2.4. Mass attenuation coefficient for construction materials. Red vertical lines mark E$_\gamma$=170 keV (backscattering at $\theta = 180°$) and E$_\gamma$=511 keV [13].

In Figure 2.5 the behaviour of $i_B(x)$ for water, sand, paper and paraffin is very similar, the value for which the backscattered intensity becomes a straight line is approximately 0.38 for all materials, this value corresponds to the last column in the Table 2.1. The thickness x at which the value of $i_B(x)$ is achieved is called the saturation thickness. Regarding paraffin and paper in Table A.4, their μ_{ph} and μ_C are very similar to those of water, therefore its i_B should overlap with that of water. This figure also means that there should not be much contrast in the Compton Camera between water and dry sand for equal thickness.

In Figure 2.6 we can see that the behaviour of $i_B(x)$ for each one of the elements is very different, in heavier elements such as lead and tungsten Equation (2.8) becomes a straight line in the first millimeters, for elements with similar Z like iron and copper the saturation thickness is approximately 2 cm. If we take a block of lead and we put up an iron object and take a picture with the Compton Camera we could distinguish the two materials since according to Table 2.1 the backscattered intensity difference is about one order of magnitude between the two materials. Using this method we can study a structural damage in a concrete wall of about 2 cm as we can see in Figure 2.7.

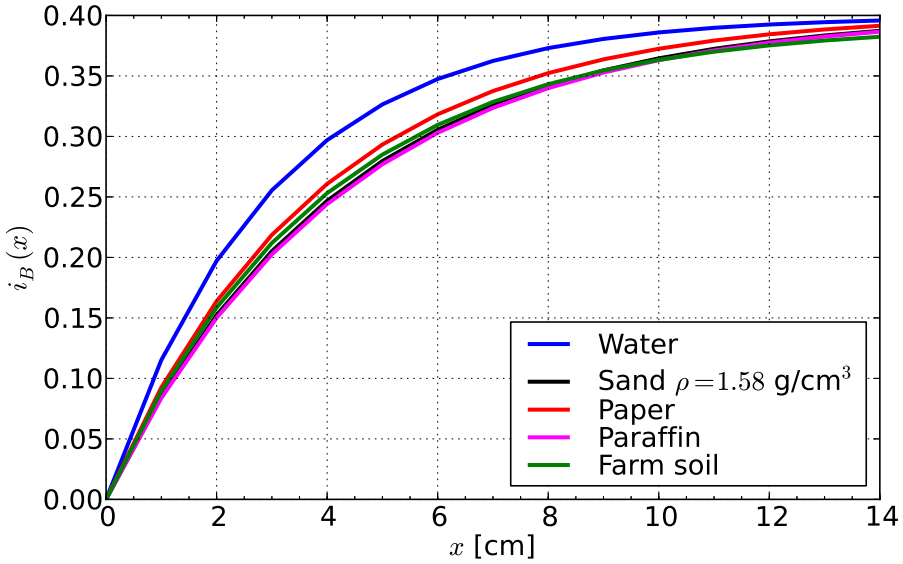

FIGURE 2.5. Behaviour of Equation (2.8) for organic materials.

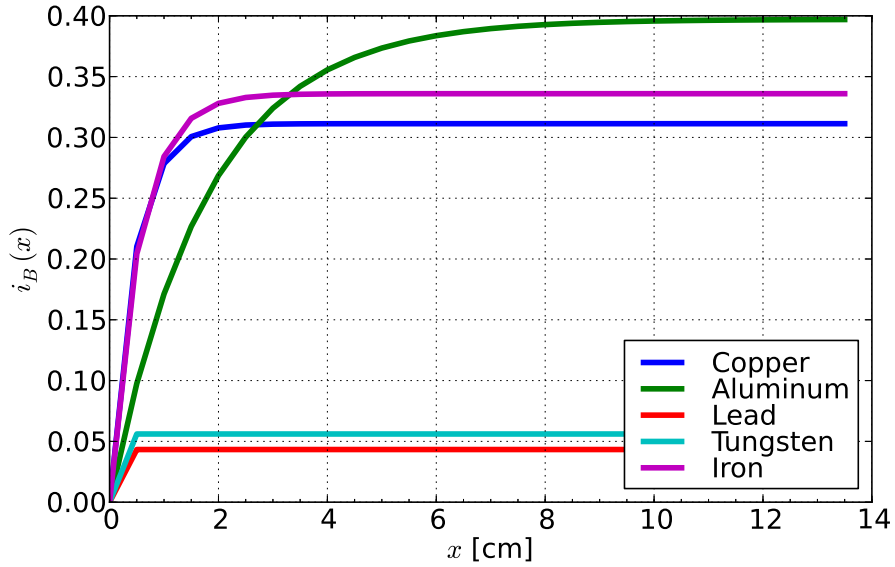

FIGURE 2.6. The scattering in Pb comes from the first milimeters.

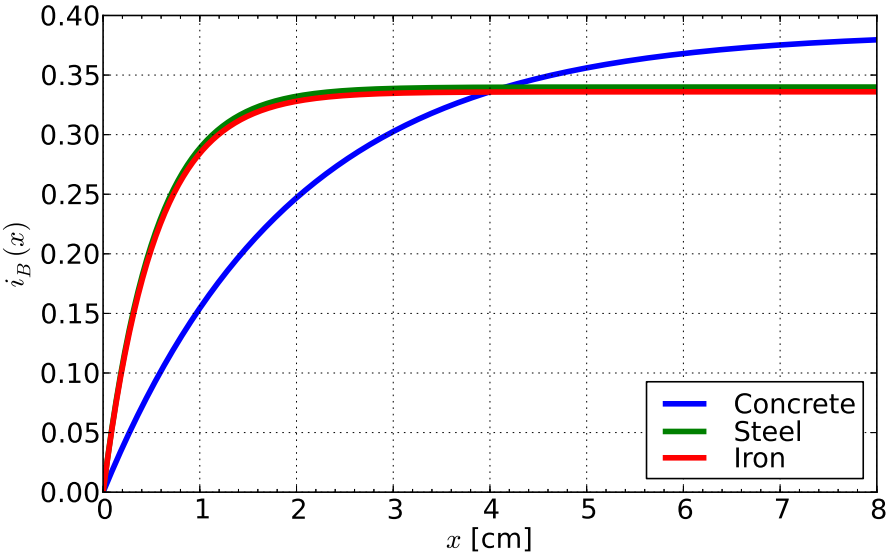

FIGURE 2.7. Behaviour of Equation 2.8 for construction materials.

CHAPTER 3

Experimental Setup

3.1 Geometrical Set-up

The schematic arrangement of the experimental set-up used for the backscattering experiments is shown in Figure 3.1. Twenty-four sheets of iron (32 × 20) cm^2 and fourteen sheets of aluminum with the same dimensions were used like samples.

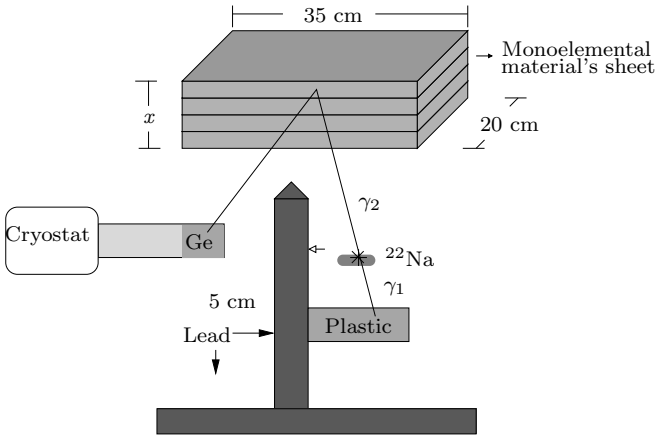

FIGURE 3.1. Set-up used for the backscattering experiments. It uses a Ge detector a plastic scintillator, ^{22}Na source and some sheets of monoelemental material.

A ^{22}Na source is placed at about 19 cm to the sample. The source used is an IDB Holland standard sealed ^{22}Na, model CAL2600 with an activity 0.46 MBq in October 2012. Below the sample, the Ge detector is placed, next to the γ source. The detector used is a Canberra GC109 coaxial germanium detector of 4.65 cm of diameter and 4.75 cm of length attached to a Canberra Big Mac cryostat. The Ge detector has an energy resolution of 1.9 keV at 1.33 MeV. 13 cm from the source a plastic scintillator is fixed. In this case a Scionix Holland plastic scintillator detector, coupled to an Ortec photomultiplier base with preamp and power supply

is used. The size of this detector is 5 cm in diameter and 5 cm in length. A lead wall 5 cm thick is placed between the source and the Ge detector in order to avoid γ-rays to directly reach the detector. The Ge detector is separated 8 cm from the lead wall in order for γ rays to be able to interact with the full volume detector.

^{22}Na decays by emitting a positron and a 1274.5 keV γ-ray as shown in the decay scheme of Figure 3.2. When the positrons interacts with an electron of the medium, both of them annihilates and produces two γ rays of 511 keV traveling in opposite directions. One of these rays can go to the plastic detector while the other one goes in the direction of the sample and may interact with it and be backscattered in the direction of the detector. By connecting the Ge detector and the plastic scintillator in time coincidences, the energy spectrum recorded by the Ge detector allows us to study the backscattering of radiation in sample. The measurement time for the backscattering spectra was of 2700 s for each sheet of monoelemental material. It is to note that for backscattering the 1274.5 keV γ-ray coming from the ^{22}Na source will contribute to accidental coincidences and thus will represent a background for all measurements. Although connecting the detectors in time coincidences reduces this contribution, it will always be present in the spectra.

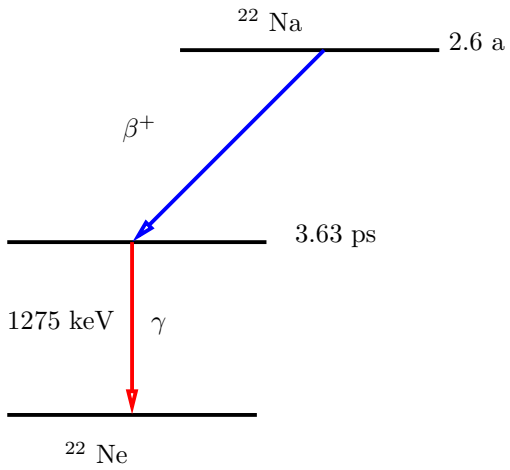

FIGURE 3.2. Decay scheme of ^{22}Na

3.2 Electronic Set-up

A sequence of electronic modules converts the charge produced by the radiation inside the detector into a signal in order to extract the information carried by each pulse. Figure 3.3 shows the block diagram of the fast coincidences electronic configuration. This set-up was previously configured in [10] and it was used in [12].

We explain the electronic setup by division of this in three electronic lines:

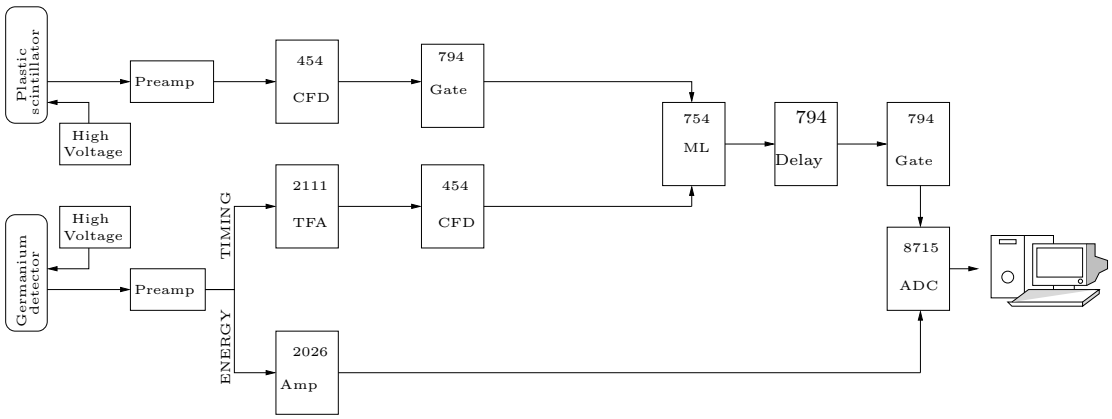

FIGURE 3.3. Block diagram of the electronic configuration of fast coincidences

1. Plastic line

The voltage applied to plastic scintillator is 1000 V. The charge pulse must be converted in a voltage pulse, this is done in a preamplifier [1].

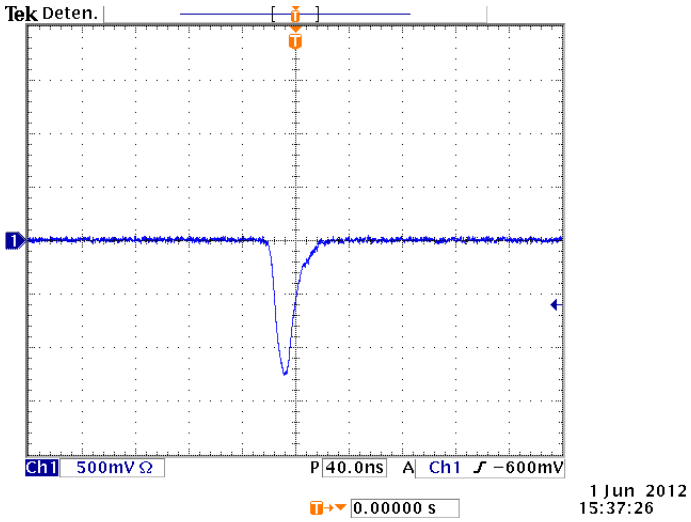

FIGURE 3.4. Output pulse from the preamplifier of the plastic detector.

Figure 3.4 shows the output pulse from the preamplifier of the plastic detector. The plastic detector is a very fast detector, the rise time is around 7 ns. The preamp output pulse of the plastic scintillator is fed into a Constant Fraction Discriminator (CFD) Model 454 to obtain a square pulse. In this case the delay time selected for this detector was 5.4 ns.

In Figure 3.5 the green lines are the output pulses of the CFD. We can see from the Figure the repetitions of the square pulse which is called jitter time effect. In order to reduce this effect the logic output pulse of the CFD goes

[1]The preamplifier or preamp is the first stage of pulse processing after the detector itself. Besides converting the charge signal into a voltage signal, the preamp also couples the impedance of the detector and the subsequent modules and reduces the noise in the detection system

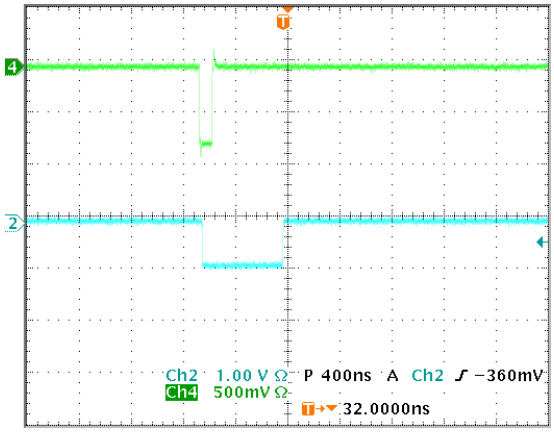

FIGURE 3.5. Output pulse from CFD of the plastic detector.

to a Phillips quad gate/delay generator Model 794 [2], the width of the signal (cyan line) in Figure 3.5 is set to cover all the jitter time. The logic square pulse of about 600 ns width was used as a time stamp for the plastic scintillator.

2. Ge timing line

The voltage applied to HPGe detector is 3500 V. In the preamplifier the charge pulse is converted in a voltage pulse. The rises times of signals coming from Ge are about some μs. These rises times depends on the specific place inside the crystal where each photon interacts. The Ge detector is a slow detector and it has a high energy resolution. Figure 3.6 shows a typical output pulse from the Ge preamplifier.

To obtain the information about the time of occurrence of the event the output labelled as Timing is used. This signal is fed into a Canberra Timing Filter (TFA) Model 2111 [3] in order to make it narrower as we can see in Figure 3.7. The signal coming from TFA is fed into the CFD to obtain a logic pulse indicating the moment of occurrence of the interaction. The delay of the signal is 50 ns. This output can be used as a time stamp for the germanium detector.

[2]Gate/Delay generators are devices which generate variable width gate pulses or delayed gates in a range from a few nanoseconds to few seconds. The desired width or delay can be selected by turning a front panel screw while viewing the signals on the oscilloscope. Gate generator functionality is required when the logic output pulse from another module needs to be re-shaped, while delay functionality is used to optimize timing experiments using fast and slow detectors.

[3]The Timing Filter Amplifier is the module in charge of pre-processing the signals from slow detectors like semiconductors. charge of this pre-processing of slow signals. This module consist of a single RC-CR stage which helps shaping the signal into a narrower pulse.

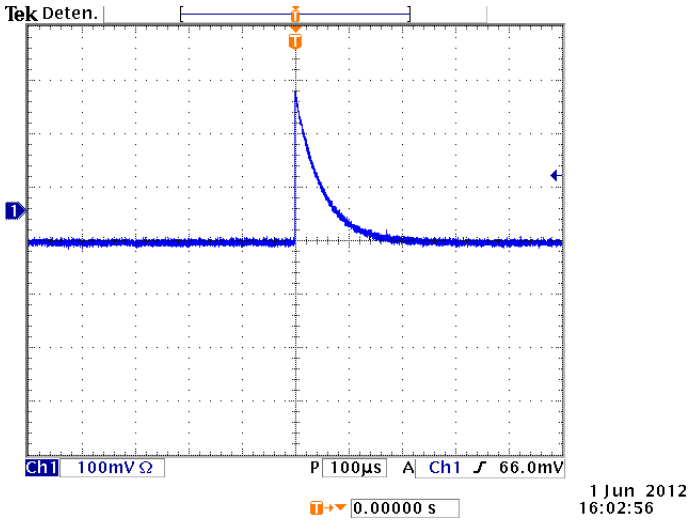

FIGURE 3.6. Output pulse from the preamplifier of the Ge detector.

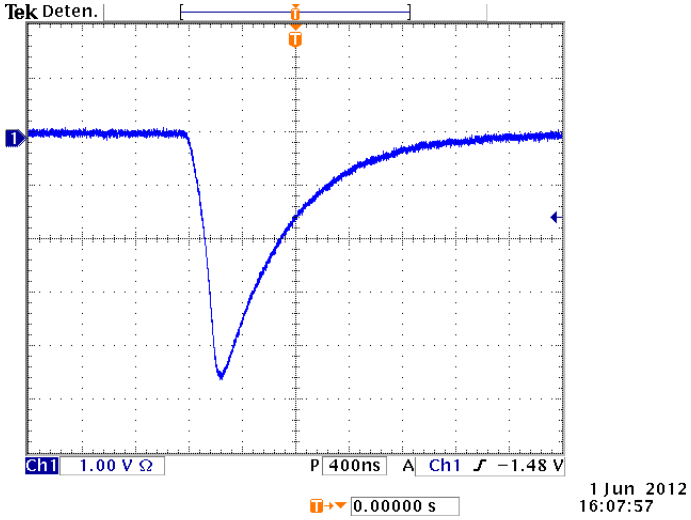

FIGURE 3.7. Output pulse from the TFA for the Ge detector.

3. Coincidence line

The next electronic stage is to compare the arrival time of the photon to each detector to determine if they arrive within certain period or time. This operation was done in the Phillips Quad Majority Logic Model 754 module [4].

The time stamps of each detector, blue line in Figure 3.8 for the Ge and cyan line in Figure 3.8 for the Plastic, are fed into the majority logic. The output pulse from the majority logic module is the magenta line in Figure 3.8 it needs to be processed by a gate/delay generator in order to give it some delay before using it in the last stage of the electronic setup.

[4]The logic pulses resulting out of on the CFD can be used to determine whether or not two events coming from different detectors occurred at the same time. The Majority logic is the electronic module in charge of this.

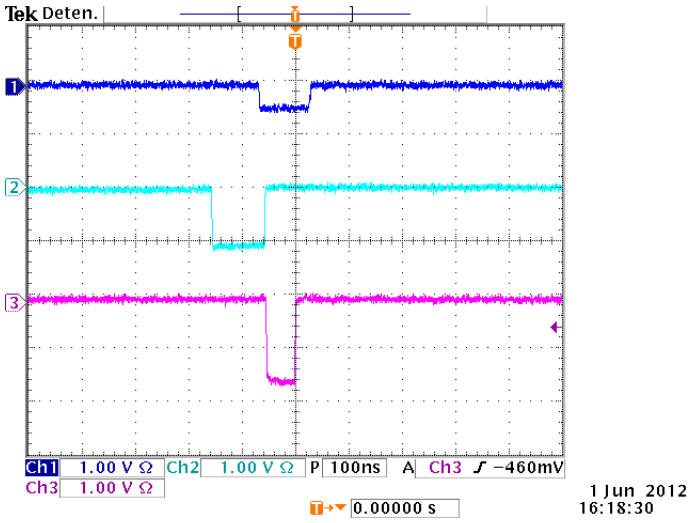

FIGURE 3.8. Output pulses from the coincidence line.

The other output signal of the Ge detector is labeled as Energy. This signal is used to obtain information about the energy deposited by radiation in the volume of the detector. This is done by feeding this signal into a Canberra Spectroscopy Amplifier Model 2026 [5], which gives a semi-Gaussian shape to the pulse with an amplitude proportional to the energy of the incident radiation. Figure 3.9 shows the semi-Gaussian signal obtained from the amplifier. This signal is fed into an ADC in order to measure the peak height.

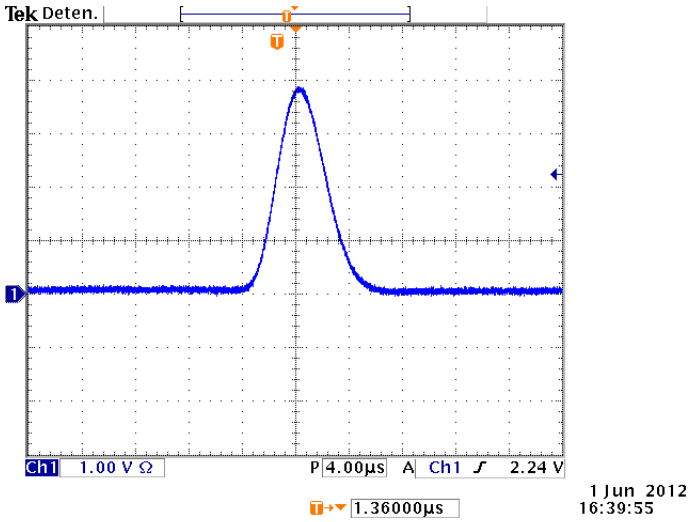

FIGURE 3.9. Output pulse of a spectroscopy amplifier.

[5] An amplifier, is an electronic device that increases the power of a signal. It does this by taking energy from a power supply and controlling the output to match the input signal shape but with a larger amplitude. In this sense, an amplifier modulates the output of the power supply.

CHAPTER 4

Results

4.1 Backscattering results

Figure 4.1 shows the backscattering spectrum for the case of having 14 sheets of aluminum. In order to analyze the spectra we can define three energy regions and study how the number of counts in each region changes when we added more sheets of aluminum. In the single backscattering region the photons have single Compton scattering in the material in angles between 123° and 154° which corresponds in energies to the range between 176.24 keV y 200.02 keV respectively. This is the range marked by dotted vertical bars in Figure 4.1. If after the first scattering the photon interacts with the material again, the scattered photon will arrive to the detector with energy lower than 176.24 keV. This is the multiple scattering region. The presence of counts at energies $E_\gamma \geqslant 200.2$ keV can be accounted for transmission of 1274 keV γ rays from the ^{22}Ne γ decay after the ^{22}Na positronic decay that succeed in passing trough the lead shielding, and reach the detector without having any interaction with the material. In Figure 4.2 is shown the energy division in the spectrum of backscattering of radiation in iron. The difference in the energy division in two materials is due to the geometry of the experimental setup. The total thickness of the aluminum sheets is 14 cm while in the iron sheets is 4.8 cm. According to Figure 3.1 the angle θ is different and therefore the scattered γ-ray energy too.

Region name	Energy range (keV)	
	Aluminum	Iron
Multiple scattering	0 - 176.2	0 - 182.0
Single scattering	176.2 - 200.0	182.0 - 199.7
Transmission	200.0 - 1300.0	199.7 - 1300.0

Table 4.1. Division of the energy regions for the backscattering spectra

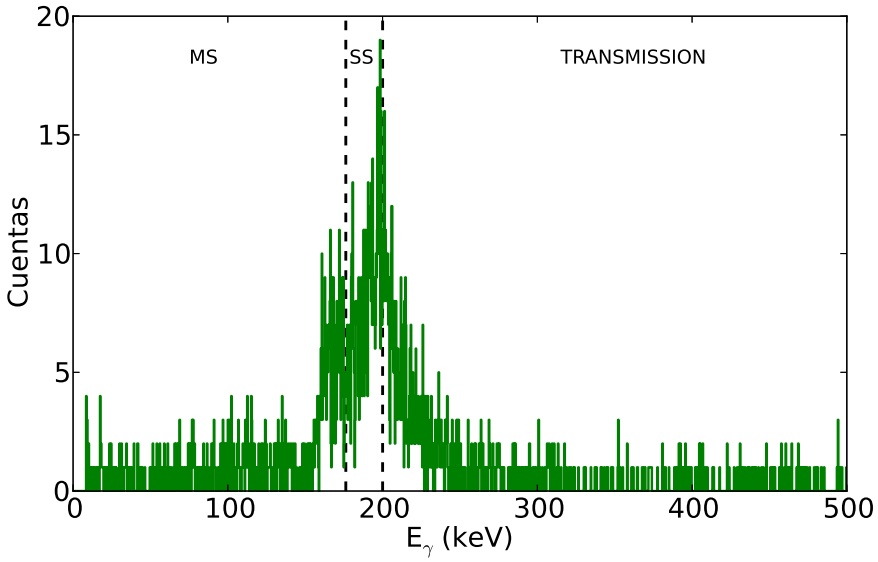

FIGURE 4.1. Spectrum of backscattering radiation in aluminum. The three different energy regions are marked by the dotted vertical lines. MS means multiple scattering region and SS means single backscattering region.

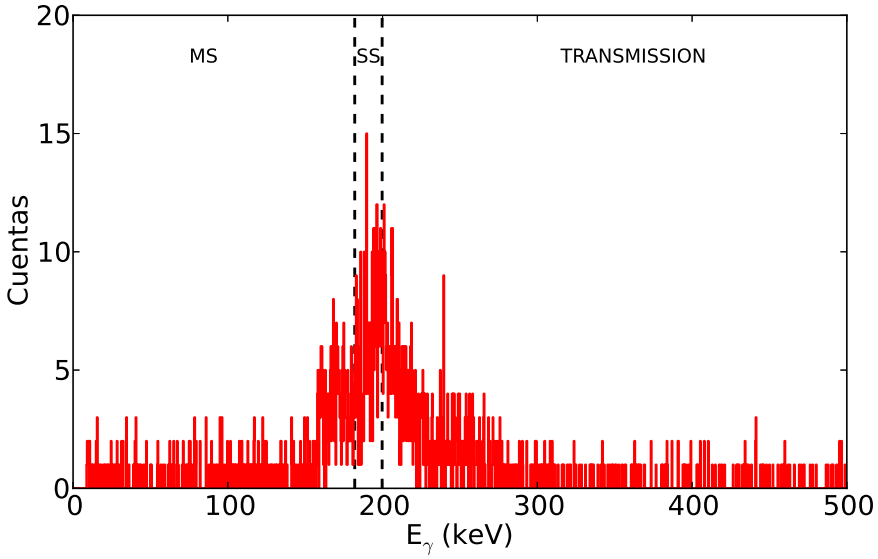

FIGURE 4.2. Spectrum of backscattering radiation in iron. The three different energy regions are marked by the dotted vertical lines. MS means multiple scattering region and SS means single backscattering region.

4.1.1 Spectroscopic analysis

In this section the spectroscopic analysis of the different energy regions is explained. We have particular interest on the highest thickness x (Figure 3.1) from

which we can obtain information of the backscattering method. After the comparison between the counts obtained and a theoretical model (Equation 2.8) is presented.

In first place we can see in Figures 4.3 and 4.4 that the total number of counts increases as material thickness increases. Even though for the first material sheets the increment is high, after some point the number of counts in the region seems to be constant. We can use this fact to define a saturation thickness for each region. The behaviour in all regions is very similar for both materials (aluminum and iron). One important question in order to study the formation in a Compton Camera is the maximum thickness x from which it is possible to extract information of the material. This is related to the saturation thickness of the regions.

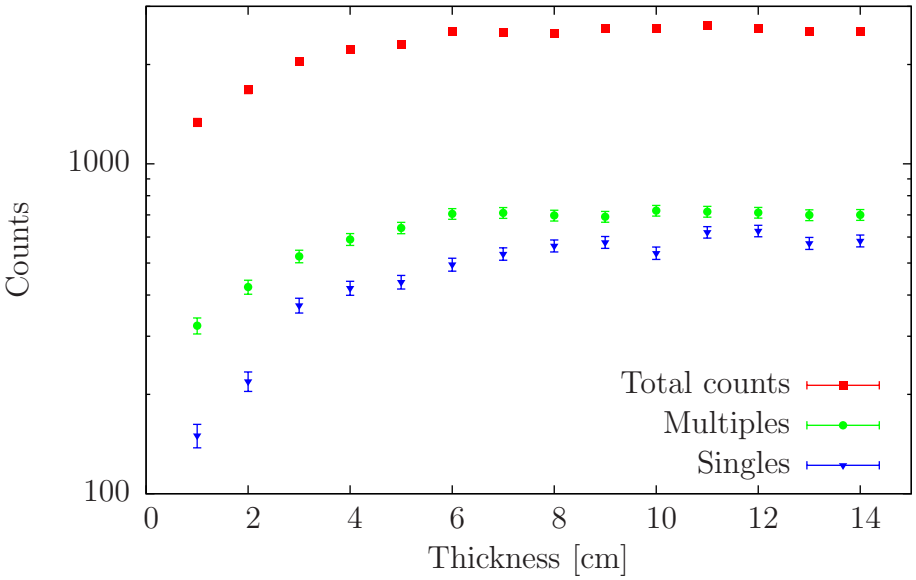

FIGURE 4.3. Number of counts in the energy regions as a function of aluminum's sheets thickness

4.1.2 Saturation thickness

The highest thickness from which we can obtain information about the material (aluminum or iron) is limited by the saturation of the number of counts in each region of the spectrum as seen in the Figures 4.3 and 4.4. According to Equation 2.8, this thickness depends on on the probabilities of interaction μ_1 and μ_2 which in turn depend on the density and atomic number Z.

In order to obtain an estimation of how thickness we can measure, an experimental saturation thickness was defined for all regions (Total, Multiple and Single). This was done by assuming that the highest number of counts achievable in a region corresponds to the number of counts obtained in the thicker sheet measured, and

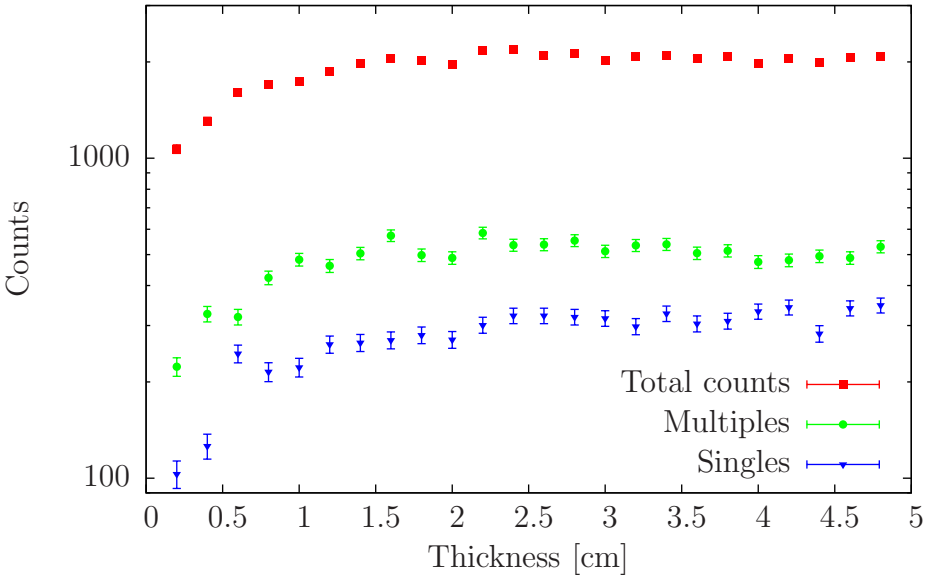

FIGURE 4.4. Number of counts in the energy regions as a function of iron's sheets thickness

searching for the thickness where 90% of this total number of counts was reached. Since there is experimental data available only for discrete values of the thickness, a linear approximation was assumed between each pair of adjacent experimental points to be able to define more precisely the saturation thickness. We can have a first approximation in the saturation thickness of each region by making an average of the experimental data obtained. Table 4.2 shows this mean values for each of the regions of the spectrum both for aluminum and for iron.

The Table indicates that the thickness we can go with methods that use only single backscattered photons in aluminum is approximately 6.8 cm. As discussed in Introduction, a device interested mainly in the single backscattered photons is the Compton Camera, which allows us to obtain images from the subsoil. It would be possible to obtain information of material layers, but it will imply to increase the measurement time or increase the energy and to perform image analysis in order to subtract the counts from upper layers and to remove the contribution of multiple scattered photons. For the case of iron, the saturation value of single backscattered photons is around 2.31 cm, indicating that in this type of material the saturation thickness is lower than saturation thickness in aluminum. With these results, we realize that we can use this method to characterize all materials and compounds proposed in the Table 2.1 and to determine in what kind of materials can we obtain images using the Compton Camera?.

In Chapter 2 we studied the theoretical model for backscattering intensity as a function of thickness for different materials and we saw that it was possible using this model to characterize the properties of materials. In Figure 4.5 is shown the

Region	Saturation thickness (cm)	
Region	Aluminum	Iron
Total counts	4.6(6)	1.22(3)
Single backscattering	6.8(7)	2.31(5)
Multiple scattering	4.8(4)	1.27(6)

TABLE 4.2. Mean value of the saturation thickness for each region of the spectrum. Results are presented both for aluminum and iron

comparison between the experimental data for aluminum and theoretical model (Equation (2.8)). The differences between them are due to several approximations in the model: first, experimental setup assumed in the model did not include a coincidences setup as we used in the experiments shown here. Second, in the model we assumed that the energy of all backscattered photons is 170 keV. In Section 4.1.2 we saw that the final photons energy are between (176.2 - 200.0) keV (Table 4.1). We can also observe that in Figure 4.5, 4.6 the number of counts is less than 3000 that is due to low activity of the source (0.46 MBq) at the date of data collection. The detector used was a Germanium detector, as discussed in Chapter 1, the efficiency of these detectors is less than the Scintillation detectors, therefore it would be advisable to improve the statistics of the data using a source with higher activity and a scintillator detector for the upcomming experiments.

In Figures 4.5, 4.6, 4.7, 4.8 the values of $\mu_{C\,1}/\mu_1 + \mu_2$ and $(\mu_1 + \mu_2)$ of Equation 2.8 were adjusted to check that the theoretical model fits correctly the experimental data obtained in this work for iron and aluminum. In Figures 4.5 and 4.6 the adjustment errors are larger than the errors reported in Figures 4.7, 4.8.

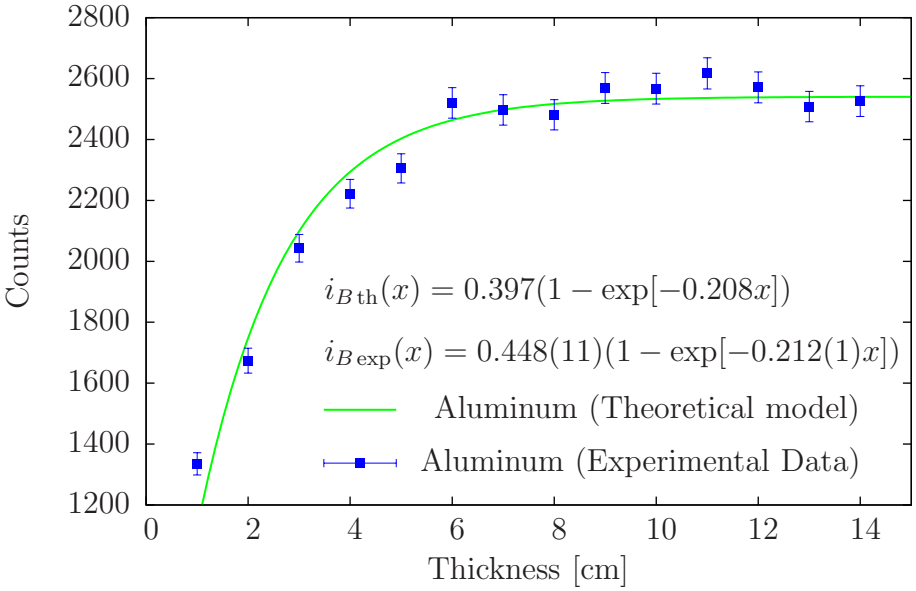

FIGURE 4.5. Comparison between the total counts of backscattering spectra for aluminum's sheets and theoretical model

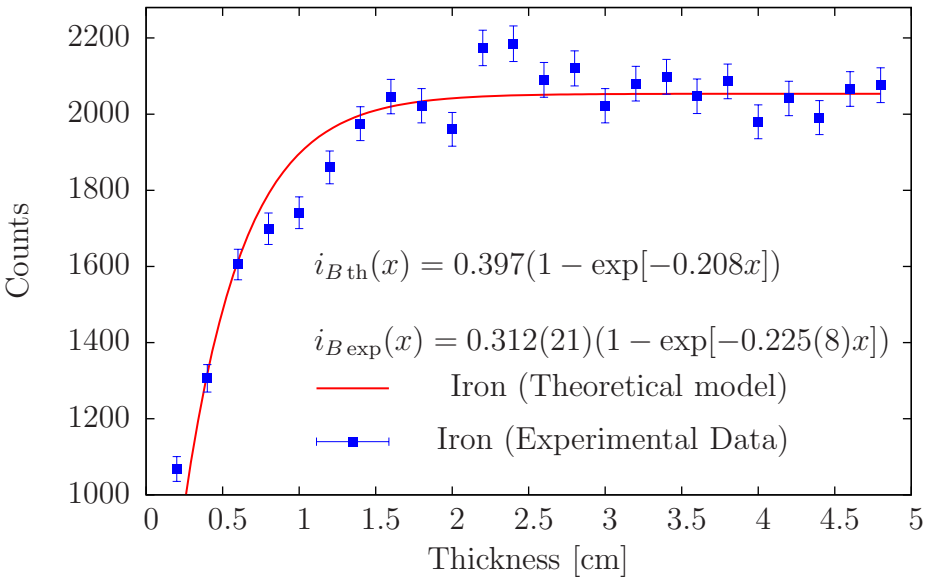

FIGURE 4.6. Comparison between the total counts of backscattering spectra for iron's sheets and theoretical model

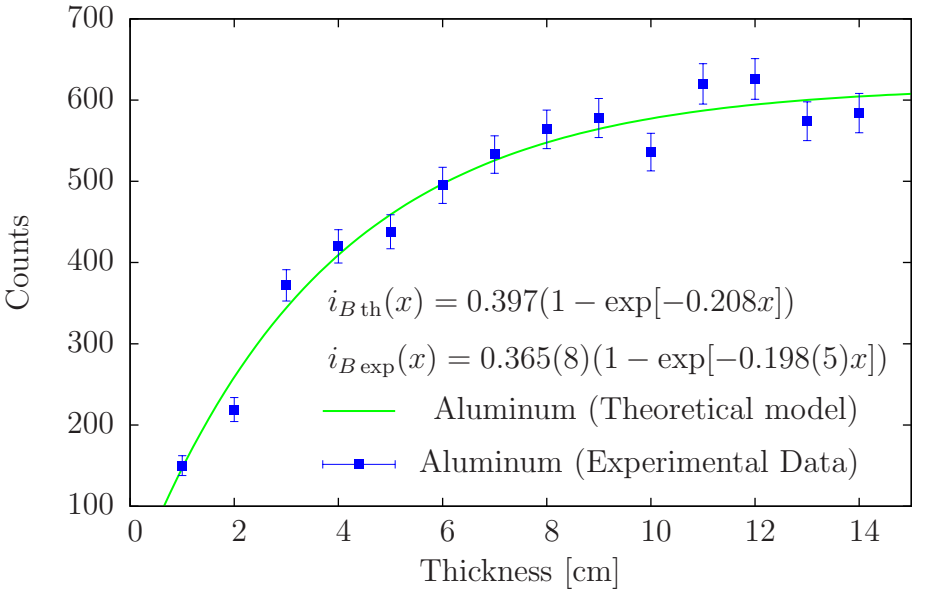

FIGURE 4.7. Comparison between the single counts of backscattering spectra for aluminum's sheets and theoretical model

We define the contrast in Chapter 2 like the difference in the backscattered intensity as a function of the thickness $i_B(x)$ between two materials.The values of $i_B(x)$ for aluminum and iron according to Table 2.1 are different in 0.06. Figure 4.9 shows the comparison of experimental data for iron and aluminum. So we concluded that we can have "contrast" in obtained images with Compton Camera between these materials.

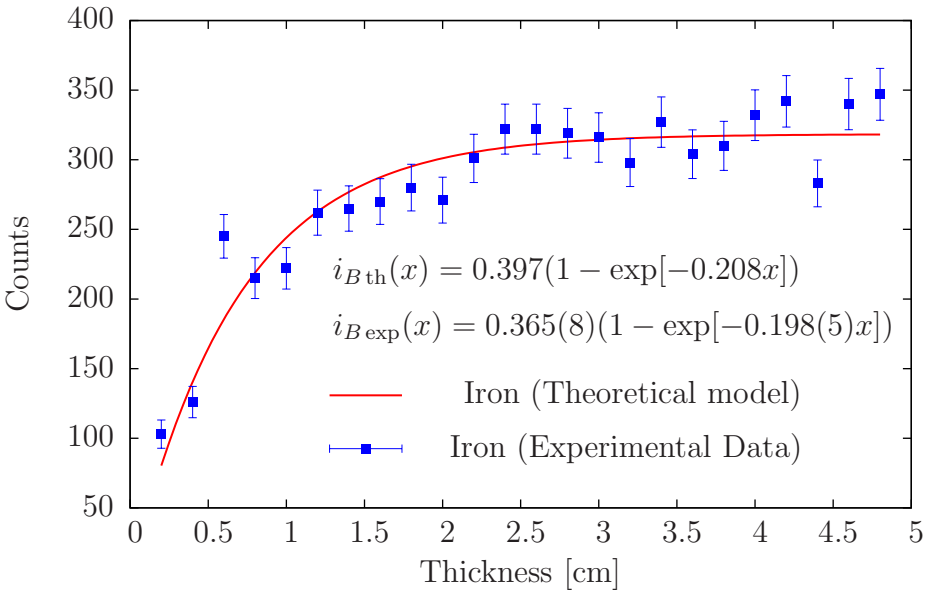

FIGURE 4.8. Comparison between the single scattering counts of backscattering spectra for iron's sheets and theoretical model

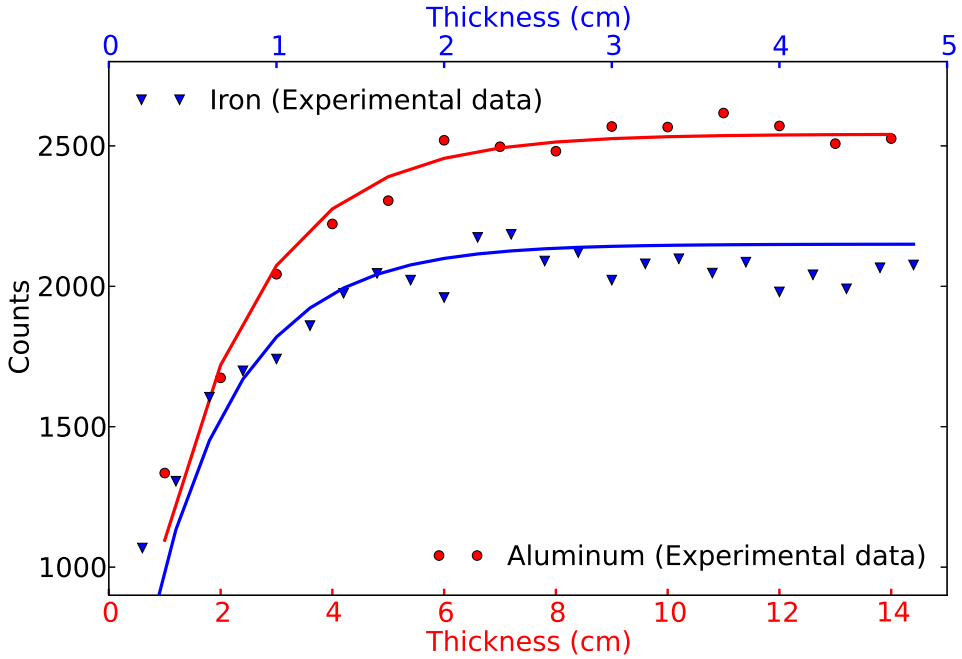

FIGURE 4.9. Comparison between the single scattering counts of backscattering spectra for iron's sheets and theoretical model

As said in Section 4.1.2 if we want to increase the saturation thickness, we can increase the energy of the incident γ ray. Using the idea proposed in Figure 2.1 but change E_γ we can study the saturation thickness as a function of energy. The plots of observed number of multiply backscattered events (having energy equal to singly scattered ones) for different incident photon energies as a function of target

thickness are shown in Figure 4.10. The curves show that for each of the incident photon energy, the numbers of multiply backscattered events increases with increase in target thickness and then saturate after a particular value of target thickness, called saturation thickness. The saturation of multiply backscattered photons is due to the fact that as the thickness of target increases, the number of scattered events also increases but on the other hand enhanced self- absorption results in decrease of the number of photons coming out of the target. So a stage is reached when the thickness of the target becomes sufficient to compensate the above increase and decrease of the number of photons. The calculated saturation thickness in Table 4.3 for multiply backscattering of gamma ray photons is found to be increasing with increase in incident gamma photons energy. This is because the penetration of gamma ray photons decreases with increase in incident gamma ray energy, so the backscattered radiation has to propagate through a large thickness and the flux of multiply backscattered photons having energy equal to the singly backscattered photons reduces. So if we increase the energy, the saturation thickness also increases so we could use the method to study materials that are thicknessly buried.

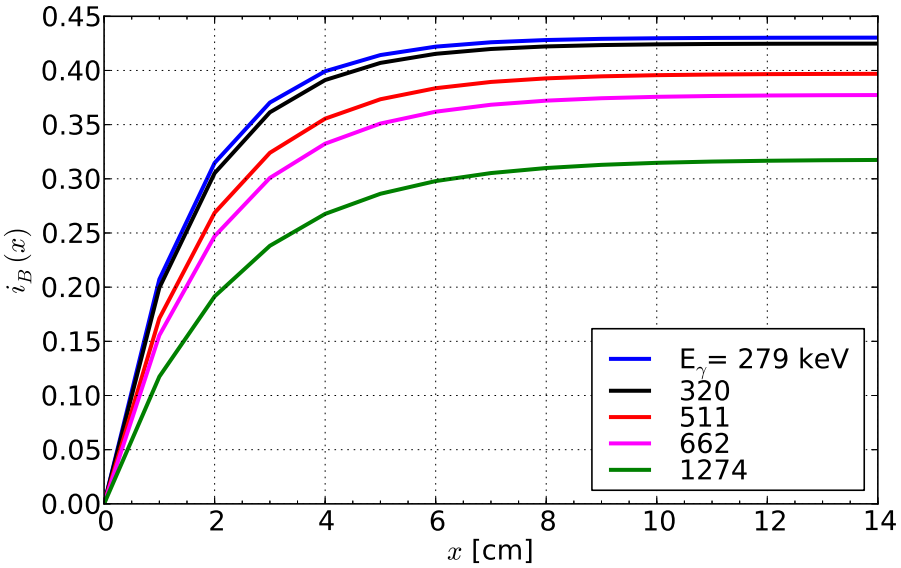

FIGURE 4.10. Variation of calculated numbers of multiply scattered events as a function of thickness of the aluminum target for different incident photon energies.

Energy (keV)	Saturation thickness (cm)
279	3.51(2)
320	3.69(3)
511	4.45(1)
662	4.98(2)
1274	6.81(4)

TABLE 4.3. Mean value of the saturation thickness for each region of the spectrum.

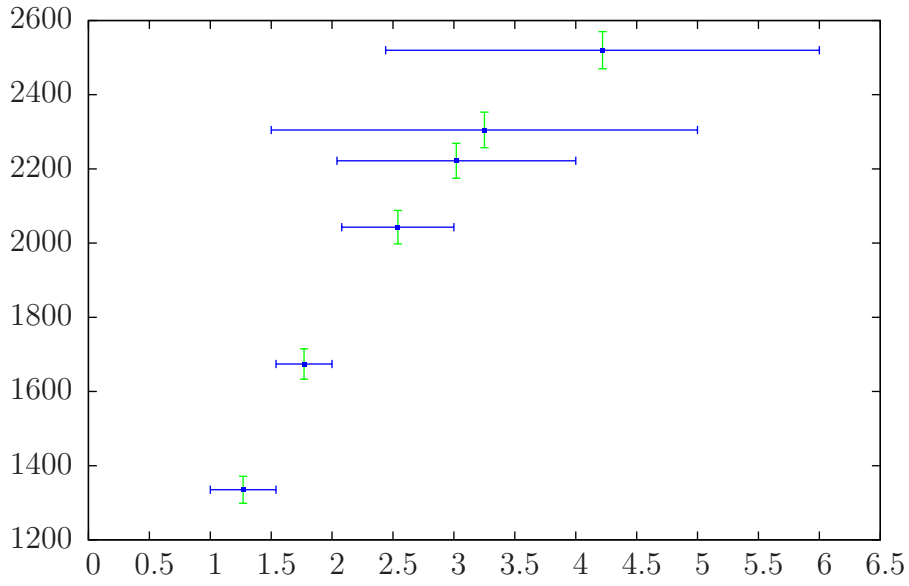

FIGURE 4.11. Calculated thickness from an aluminum object using theoretical model (Equation 2.8)

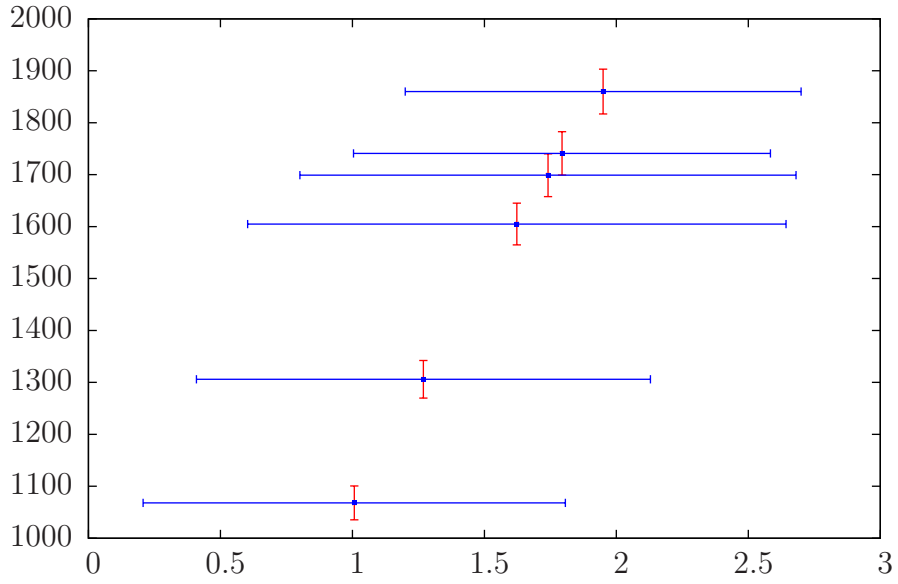

FIGURE 4.12. Calculated thickness from an iron object using theoretical model (Equation 2.8)

We realized that it is possible to evaluate the differences of backscattered intensity for different materials using the simple theoretical approximation (Equation 2.8). But using this method it is possible to develop another applications, for example from Equation 2.8 we could estimate the thickness of some material knowing its Stoichiometry. We use the same experimental setup shown in Figure 2.1 we obtain the value of i_B, using the NIST database we can have the values for μ_1, μ_2 and μ_{C1}. Using the experimental data for Iron and Aluminum we calculate these values as

shown in Figure 4.11, 4.12. The error bars shown in Figures corresponds to the standard deviation of the experimental data. We can see in Figure 4.11 that for data with Aluminum is possible to evaluate the thickness of materials with less than 4.8 cm about that comparing with Table 4.2 corresponds the saturation thickness of aluminum to an energy of 511 keV. This happens because the thickness from the saturation value of the backscattered intensity at each point is similar.

APPENDIX A

Stoichiometry

Element or Compound	Concentration (%)
SiO_2	96.18 %
Al_2O_3	1.21 %
TiO_2	0.23 %
Fe_2O_3	0.19 %
CaO	0.05 %
K_2O	0.05 %
Na_2O	0.04 %
P_2O_5	0.03 %
Zr	216 ppm
S	37 ppm
Sr	28 ppm
Ni	24 ppm
Zn	15 ppm
Pb	11 ppm
Rb	9 ppm

TABLE A.1. Sand composition obtained by XRF

Element or Compound	Concentration (%)
SiO_2	60.57 %
Al_2O_3	12.89 %
Fe_2O_3	2.40 %
CaO	1.54 %
MgO	0.69 %
TiO_2	0.57 %
P_2O_5	0.51 %
K_2O	0.49 %
MnO	0.04 %
Ba	476 ppm
S	244 ppm
Zr	191 ppm
Sr	162 ppm
V	118 ppm
Zn	116 ppm
Cr	86 ppm
Pb	44 ppm
Cu	31 ppm
Rb	23 ppm
Ni	20 ppm

TABLE A.2. Farming soil composition obtained by XRF. We can see that it is mainly SiO_2 although other compounds are also important. The components do not sum 100% as some organic matter and the heavy elements concentration cannot be determined with XRF.

Compound	Concentration (%)
Ca_3SiO_5	50 %
Ca_2SiO_4	25 %
$Ca_3Al_2O_6$	10 %
$Ca_4Al_2Fe_2O_{10}$	10 %
$CaSO_42H_2O$	5 %

TABLE A.3. Concrete's chemical composition [16].

Materials	$\mu_{C\,1}$ (cm^2/g)	$\mu_{ph\,1}$ (cm^2/g)	$\mu_{T\,1}$ (cm^2/g)	$\mu_{C\,2}$ (cm^2/g)	$\mu_{ph\,2}$ (cm^2/g)	$\mu_{T\,2}$ (cm^2/g)
Sand	0.08605	0.000092	0.08614	0.12700	0.00242	0.129420
Water	0.09575	0.000018	0.09577	0.14220	0.00049	0.142687
Paper	0.09150	0.000013	0.09151	0.13590	0.00035	0.136250
Paraffin	0.09890	0.000005	0.09891	0.14710	0.00015	0.147253
Soil	0.08460	0.000334	0.08493	0.12610	0.00427	0.130370
Copper	0.07820	0.002420	0.08062	0.11360	0.05700	0.170600
Aluminum	0.08299	0.000126	0.08312	0.12250	0.00335	0.125849
Lead	0.06670	0.078400	0.14510	0.09270	1.30300	1.395700
Tungsten	0.06800	0.056500	0.12450	0.09516	0.99320	1.088360
Concrete	0.08570	0.000379	0.06080	0.12640	0.00949	0.135890
Steel	0.08035	0.001550	0.08190	0.11720	0.03726	0.154460
Iron	0.07993	0.001665	0.08160	0.11640	0.03992	0.156320

TABLE A.4. Mass attenuation coefficients read out from Figures 2.2, 2.3, 2.4 [13].

Bibliography

[1] G. Harding, B. Schreiber. *Coherent X-ray scatter imaging and its applications in biomedical science and industry. Rad. Phys. Chem* (1999) 229:245.

[2] Martens, G., Bomsdorf, H., Harding, G., Kanzenbach, J., Linde, R., 1993. Coherent x-ray scatter imaging for foodstuff contamination detection. SPIE 2092, 387-398.

[3] Strecker, H., Harding, G., Bomsdorf, H., Kanzenbach, J., Linde, R., Martens, G. *Detection of explosives in airport baggage using coherent x-ray scatter.* SPIE 2092, 399-410.

[4] J. Gerl, F. Ameil, I. Kojouharov and A. Surowiec, *High-resolution gamma backscatter imaging for technical applications*, Nuclear Instruments and Methods in Physics Research A **525** (2004), 328–331.

[5] J. Gerl. *Gamma-ray imaging exploiting the Compton effect.* Nuclear Instruments and Methods in Physics Research A, **752** (2005) 688.

[6] E. Fajardo, M. F. Nader, F. Cristancho, and J. Gerl, *The photographic capacity of a gamma compton backscattering device*, American Institute of Physics Conference Proceedings **1265** (2010), 449–450.

[7] Natalia González, *Caracterización de un dispositivo para obtención de imágenes por retrodispersión Compton.*, Undergraduate thesis, Universidad Pedagógica y Tencológica de Colombia, 2010.

[8] N. González, E. Fajardo, W. Blanco and F. Cristancho , *Characterization of a γ-backscattering imaging device*, American Institute of Physics Conference Proceedings **1423** (2012), 359–362.

[9] M. L. Cortés, L. M. Melo and F. Cristancho, *Influence on humidity on the scattering of γ-rays in soil*, American Institute of Physics Conference Proceedings **1265** (2010), 395.

[10] Martha Liliana Cortés, *Energy and time characterization of the response of the soil to γ-rays.*, Master's thesis, Universidad Nacional de Colombia, 2010.

[11] J. Gómez-Muñoz, M. L. Cortés, and F. Cristancho, *Gamma backscattering in soil layers with different thickness and water content.*, American Institute of Physics Conference Proceedings **1265** (2012), 418–421.

[12] Juansebastian Gómez Muñoz, *Estudio de la restrodispersión γ en capas de suelo con diferente espesor y contenido de agua.*, Undergraduate Thesis, Universidad Nacional de Colombia, 2012.

[13] International Atomic Energy Agency, *Development of protocols for corrosion and deposits evaluation in pipes by radiography*, Industrial Applications and Chemistry Section. International Atomic Energy Agency. (2007).

[14] Nuclear Energy Institute
`http://www.nei.org/How-It-Works/industrialapplications`

[15] Photon cross section database
`http://physics.nist.gov/PhysRefData/Xcom/html/xcom1-t.html.`

[16] O. Klein, Y. Nishina. *Uber die Streuung von Strahlung durch freie Elektronen nach der neuen relativistischen Quantendynamik von Dirac.* Z. Phys. **52** (11-12): 853-869 (1929).

[17] H. Nakamura1, Y. Shirakawa, S. Takahashi and H. Shimizu. *Evidence of deep-blue photon emission at high efficiency by common plastic.*, Europhysics Letters **95** 22001 (2011).

[18] S. W. Moser, W. F. Harder, C. R. Hurlbut, M. R. Kusner. *Principles and practice of plastic scintillator design.*, Radiation Physics and Chemistry **41** 31-36 (1993).

[19] Glenn F. Knoll. *Radiation Detection and Measurement.* John Wiley & Sons, Inc., third edition, 2000.

[20] Willian Leo, *Techniques for Nuclear and Particle Physics Experiments*, Springer-Verlag, 1994.

[21] `http://mdmetric.com/tech/chempropi.htm`

[22] `http://physics.nist.gov/PhysRefData/XrayMassCoef/ComTab/concrete.html`